

# **Test-beam analysis and TCAD simulation of the HV-CMOS pixel technology proposed for the ATLAS experiment at the HL-LHC**

THÈSE de Master

par

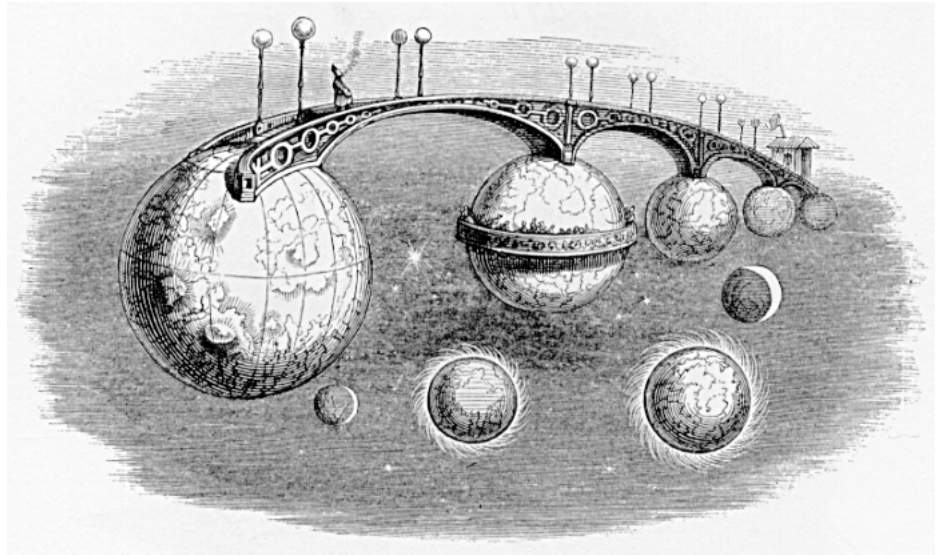
**Francesco Armando Di Bello**

de  
Gaeta (Italie)

GENÈVE  
2015



*A mia madre.*



J. J. Grandville, *Un autre Monde*.





## **Acknowledgements**

First, I want to express my gratitude to Prof. Giuseppe Iacobucci who gave me the opportunity to participate to this international and challenging research project.

My gratitude also goes to Dr. Mathieu Benoit and Dr. Sergio González Sevilla for their precious advices and patience in having an accurate concern during the work done on my thesis.

Furthermore I would like to thank Javier Bilbao for introducing me to the test-beam reconstruction as well for the support on the way. I would also thank Antonello Miucci for the stimulating debates. Thank you also to my family for supporting me pursuing my dreams, and to Sara, who dreams with me.



---

## Table of Contents

---

<b>1</b>	<b>The ATLAS detector</b>	<b>3</b>
1.1	The Large Hadron Collider . . . . .	3
1.2	The ATLAS detector . . . . .	4
<b>2</b>	<b>Principles of silicon detectors</b>	<b>11</b>
2.1	Interactions of charged particles with matter . . . . .	11
2.2	Semiconductor properties . . . . .	13
2.3	The pn-junction . . . . .	14
2.4	The SRH model . . . . .	17
2.5	Radiation damage in silicon devices . . . . .	18
<b>3</b>	<b>The HV-CMOS pixel technology</b>	<b>21</b>
3.1	The FE-I4 chip . . . . .	21
3.2	The HV-CMOS pixel technology . . . . .	23
<b>4</b>	<b>Test-Beam results</b>	<b>27</b>
4.1	The FE-I4 Telescope . . . . .	27
4.2	The off-line reconstruction software . . . . .	27
4.3	Telescope simulation . . . . .	32
4.4	Results . . . . .	33
<b>5</b>	<b>TCAD simulations</b>	<b>41</b>
5.1	The model layout . . . . .	41
5.2	Physics model . . . . .	43
5.3	Results . . . . .	44
<b>6</b>	<b>Appendix</b>	<b>53</b>



A High Luminosity upgrade of the LHC (HL-LHC [1]) is foreseen to start in  $\sim 2026$ . An instantaneous luminosity of  $5 \times 10^{34} \text{ cm}^{-2} \text{ s}^{-1}$ , with the goal of reaching an integrated luminosity of  $3000 \text{ fb}^{-1}$  after 10 years of operation, is expected for the two LHC multi-purpose experiments ATLAS [2] and CMS. The long shutdown (LS3) of the collider planned for 2024 will give the possibility for an upgrade of the detectors. The inner detector of the ATLAS experiment will not cope with the large particle multiplicity at this luminosity and therefore a new tracker (ITk) must be installed. Radiation hardness and fast response in high pile-up environment are mandatory requirements in view of the HL-LHC. New particle detectors matching these specifications have been proposed based on the commercial well-established High-Voltage CMOS (HV-CMOS) technology [3]. A test-beam campaign has been performed in 2014 at the CERN PS and SPS and another one is ongoing this year (2015) at the SPS. Results show an efficiency of 99.5% for the non-irradiated sample and 96.5% for the sample irradiated at  $10^{15} \text{ n}_{eq}/\text{cm}^2$ . In view of these promising results, a new HV-CMOS prototype designed to fulfill the requirements for being considered a valid technology for the ITk is foreseen for September 2015. During the first part of this master work I have been involved in test-beam analysis which include the optimization of the off-line reconstruction software, the simulation of the telescope and the analysis of the performance of different HV-CMOS samples. Secondly, I took part in a collaboration between the University of Geneva (Switzerland), the University of Liverpool (UK), CERN (Switzerland) and LAL (France) aiming to optimize the design of the upcoming prototype using TCAD (Technology Computer Aided Design) simulations.

In the first chapter I will briefly discuss the ATLAS detector and its upgrade program. After reviewing in chapter 2 the operating principle of the silicon detectors, the main features of the HV-CMOS technology for the HL-LHC are explained in the third chapter. In the fourth chapter I will describe the test-beam results. In the fifth and final chapter I will introduce finite element simulations and their application to semiconductor physics. Specifically, I will discuss the layout of the sensor model as well as the physics model used in simulation; results such as the distribution of the electrostatic potential in the device, and transient current properties for simulation by ionizing particles crossing the bulk of the detector will be presented for different resistivities and bias voltages.



The Large Hadron Collider (LHC) is a particle collider located at the European Organization for Nuclear Research (CERN) at the border between Switzerland and France.

The ATLAS, CMS, LHCb and ALICE experiments are located at four interaction points of the LHC [4]. ATLAS and CMS are multi-purpose detectors studying the origin of the the electroweak symmetry breaking and searching for the new phenomena at the TeV scale, LHCb is an experiment devoted to the measurement of CP violation and ALICE is dedicated to the study of heavy ions collisions.

### 1.1 The Large Hadron Collider

In 2015 the LHC accelerated protons at the record center-of-mass energy of 13 TeV. Each beam is designed to have 2808 bunches, separated one from another by 25 ns and containing about  $10^{11}$  protons.

Figure 1.1 shows the accelerating system. The protons source is a container of hydrogen gas, an electric field is used to strip hydrogen atoms from their electrons to yield protons. The accelerating process starts in the linear accelerator LINAC2, which accelerates the protons to the energy of 50 MeV. The beam is then injected into the Proton Synchrotron Booster (PSB) which provides an energy of the protons of 1.4 GeV. The PSB subsequently injects the protons to the Proton Synchrotron (PS) where they are accelerated up to 25 GeV. The beam is then sent to the Super Proton Synchrotron (SPS), which accelerates the protons to 450 GeV. Finally they are injected into the LHC.

The LHC consists of radio-frequency (RF) cavities to accelerate the injected protons and 6700 magnets divided into: 1232 dipoles, which constrain the particles to follow a circular trajectory, 392 quadrupole magnets for beam focusing and higher-order multipole magnets aiming for beam correction. Technical aspects are detailed elsewhere [5].

One of the most important parameter of the collider is the luminosity which defines the number of events seen per second at each interaction region i.e.

$$\frac{dN_e}{dt} = \sigma * \mathcal{L}$$

where  $\sigma$  is the cross section of interest and  $\mathcal{L}$  is the instantaneous luminosity. For a gaussian-distributed beam containing  $n_b$  number of bunches, composed of  $N_b$  particles per bunch, interacting at a frequency  $f$ , the instantaneous luminosity can be defined:

$$\mathcal{L} = \frac{N_b^2 n_b f \gamma F}{4\pi \epsilon_\pi \beta^*}$$

where the normalised transverse emittance ( $\epsilon_\pi$ ) and the beta function at the point of the collision ( $\beta^*$ ) characterize the geometrical properties of the beam,  $\gamma$  is the usual relativistic boost factor, F is a geometrical factor





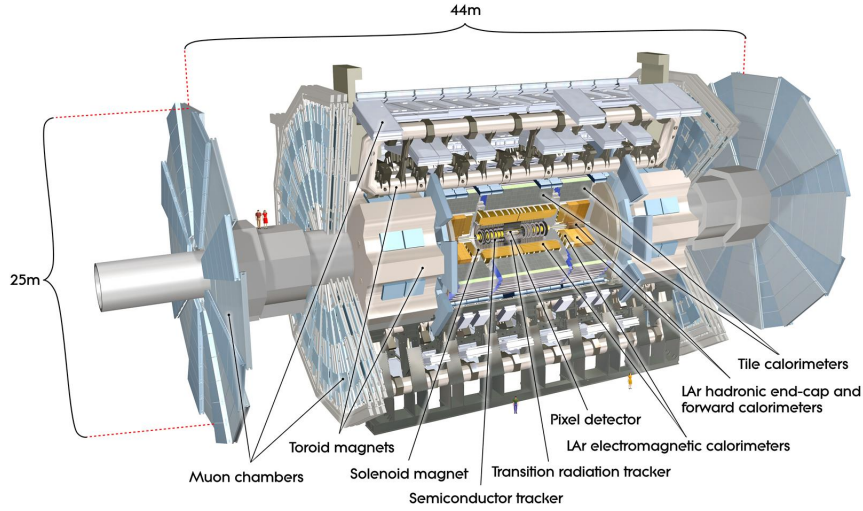


**Figure 1.2** – Artist's overview of the ATLAS detector and its sub-systems [2].

ATLAS uses a right-handed coordinate system with its origin at the center of the detector, and the  $z$ -axis along the beam line. The  $x$ -axis points from the IP to the center of the LHC ring, and the  $y$ -axis points vertically. Cylindrical coordinates  $(r, \phi)$  are used in the transverse plane,  $\phi$  being the azimuthal angle around the beam line. The pseudorapidity ( $\eta$ ) is defined in terms of the polar angle (angle w.r.t. the beam-axis)  $\theta$  as  $\eta = -\ln[\tan(\theta/2)]$ .

## Inner Detector

The Inner Detector (ID) provides the measurement of the trajectory and of the momentum of charged particles and the reconstruction of primary vertices, the point where the p-p interactions take place. It also allows the reconstruction of secondary vertices, the point where long-lived particles (e.g. B-mesons) decay.

The ID is formed by a silicon pixel detector, a silicon micro-strip detector (SCT) and straw-tube transition radiation tracker (TRT). In order to measure the momentum of the particles, the ID is surrounded by a superconducting solenoid which provides a 2 T magnetic field directed along the beam axis.

The Pixel Detector is the nearest to the beam line (at  $\sim 33$  mm radial distance) and its major contribution is in the accurate measurement of vertices. The pixel layers are segmented in  $R$ - $\phi$  and  $z$  with typically four (with IBL) pixel layers crossed by each particle.

The silicon micro-strip detector system is designed to provide eight precision measurements per charged particle in the intermediate radial range ( $\sim 400$  mm), contributing to the measurement of momentum, impact parameter and vertex position.

At a greater distance ( $\sim 750$  mm), it is located the TRT. It provides typically 30 tracking points. It is formed by straws filled with a gas mixture based on Xenon, alternating with radiators. When ultrarelativistic particles cross the radiator layers they emit X-rays which can then be detected and used to discriminate electrons from charged hadrons [6]. The Inner Detector is capable of reconstructing tracks within  $|\eta| < 2.5$ . A global vision of the ID is shown in Figure 1.3.

## The IBL

A fourth pixel layer, called Insertable B-Layer (IBL) has been installed inside the ATLAS ID during the 2014 shutdown. An upgrade of the ID was needed in order to avoid degradation of the ATLAS performance in tracking, vertex reconstruction and b-tagging due to the high luminosity ( $\mathcal{L} = 10^{34} \text{ cm}^{-2} \text{ s}^{-1}$ ) expected at the LHC and to compensate for possible failures of the ID system due to radiation damage effects. The IBL layout is shown in figure 1.4. It consists of 14 staves arranged around the beam-pipe with a tilted angle of  $14^\circ$  to

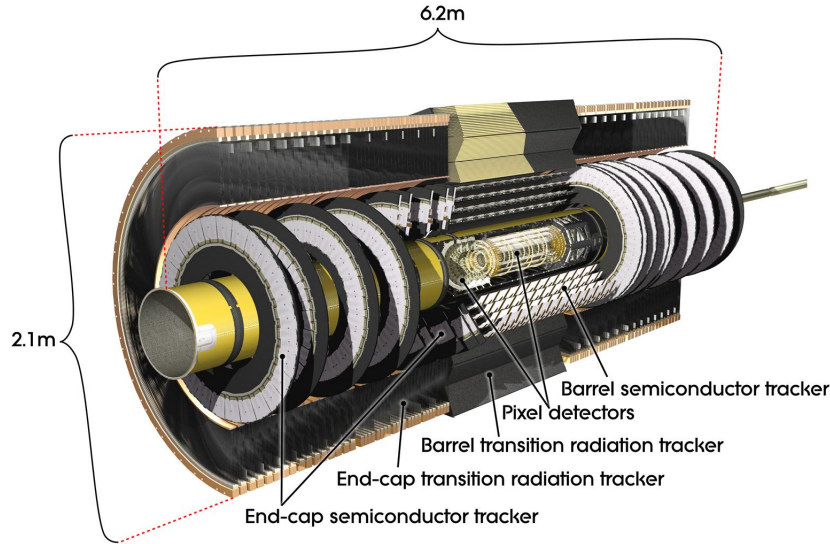


**Figure 1.3** – Overview of the ATLAS Inner Detector [6].

ensure a fully hermetic coverage and to compensate for the Lorentz angle in the 2 T solenoid magnetic field. Each IBL stave is 64 cm long and covers a pseudo-rapidity range of  $|\eta| \leq 2.9$ . The average distance of the staves with respect the center of beam pipe is around 33 mm.

The IBL is built out of two sensor technologies: planar sensors [7] which cover the innermost part of the detector for 75 % of the active area, and the novel 3D sensor [7], introduced for the first time in one of the LHC experiments, which are used in the largest  $\eta$  range of the detector, covering the 25 % of its active area [8].

Due to the extreme operating condition of the IBL, a new readout chip has been developed, the FEI4 chip [9]. It is also used to read-out the HV-CMOS sensor under investigation for this thesis and it will be described in more details in chapter 3.

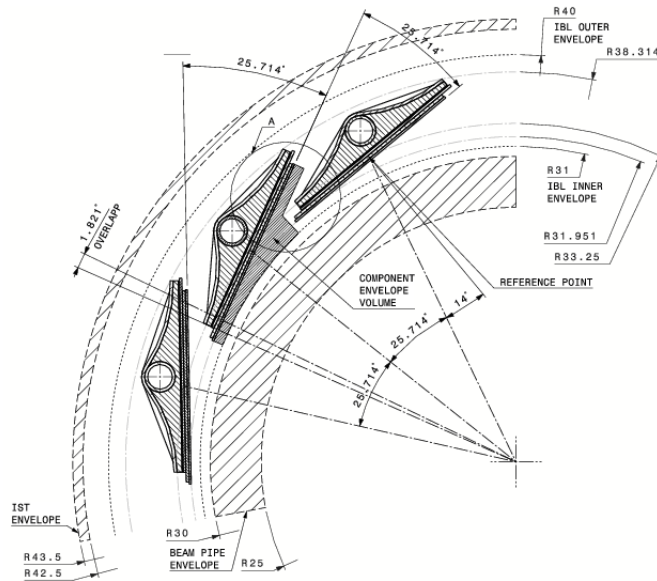


**Figure 1.4** – Layout of the Insertable B-Layer in  $r$ - $\phi$  view [8]

## The magnetic system

The magnetic field is fundamental for the measurement of the momenta of charged particles produced in the experiment.

The ATLAS magnetic system provides an almost complete coverage in pseudorapidity of the magnetic field in the Inner Detector and in the Muon Spectrometer. The ATLAS magnetic system is composed of four sub-systems: the central solenoid, the barrel Toroid and two end-cap Toroids.

The central solenoid is a superconducting magnet located around the inner detector. It is designed to provide a 2 T magnetic field in the central tracking volume and it is kept at a temperature of 4.5 K by liquid Helium. The Barrel Toroid consists of 8 flat superconducting race-track coils also kept at 4.5 K. Each of them is 25 meters long and 5 meters wide.

The two end-cap toroids, positioned inside the barrel toroid at both ends of the central solenoid, provide in the vicinity of the beam axis, the magnetic field required to deflect particles emitted at small angle from the beam [10].

## Calorimeters

The calorimetric system provides a measurement of the energy of the particles. It is composed of an electromagnetic calorimeter and a hadronic calorimeter. Both of them are sampling calorimeters, i.e. they are formed by layers of two materials: the absorber and the active material. The particle passing through the absorber material, typically causes a cascade of particles, producing electrons and photons in the electromagnetic calorimeter, and hadrons in the hadronic calorimeters, the so-called "showers".

The electromagnetic calorimeter (ECAL) is located right after the solenoid magnet and provides a measurement of the energy of electrons and photons. It is composed of accordion-shaped electrodes, providing complete coverage and symmetry in the azimuthal angle  $\phi$ , and of lead absorber plates in combination with liquid argon serving as active material. The electromagnetic calorimeter has a cylindrical shape and it is divided into a central barrel region ( $|\eta| < 1.475$ ) and two end-cap regions at both ends of the detector ( $1.375 < |\eta| < 2.5$  for the outer wheel and  $2.5 < |\eta| < 3.6$  for the inner wheel). In the region covered by the inner detector ( $|\eta| < 2.5$ ) the ECAL has three longitudinal layers. The first layer (also called presampler) has a fine segmentation in  $\eta$  to facilitate the separation of  $\gamma$  from  $\pi^0$ , as well as  $e$  from  $\pi^-$  and to improve the resolution of the shower position and direction measurement. The second layer is thickest, therefore the majority of the energy is deposited in this layer. In order to provide a good resolution in both coordinates  $\phi$  and  $\eta$  it is segmented into several towers with a square base. The third layer is specifically dedicated to high energy electrons ( $E > 50$  GeV) and has a coarser segmentation. Figure 1.5 shows an overview of the longitudinal and transverse segmentation of the ECAL.

The Hadronic calorimeter covers a wide pseudo-rapidity range. In order to optimize the measure, it uses different technologies depending on the pseudo-rapidity range. The Hadronic Tile Calorimeter (HTC) is composed of steel and scintillating tiles as absorbing and sampling material respectively. The photons produced by the active material are collected by optical fibers and converted into current by photomultipliers. It is divided in two components, the barrel section ( $|\eta| < 1$ ) and two extended barrel sections ( $0.8 < |\eta| < 1.7$ ) [11].

The Liquid Argon End-cap Calorimeter is also a sampling calorimeter: the active material is Argon and Copper has been chosen as the absorber. The Hadronic Endcap Calorimeter (HEC) is formed by two independent wheels with an outer radius of 2.03 m. It provides coverage over the  $1.5 < |\eta| < 3.2$  pseudorapidity range.

The Liquid-Argon forward Calorimeter (FCAL) covers the very forward region ( $3.2 < |\eta| < 4.9$ ). In this region the energy density of the particle is high and the FCAL is divided into three layers in order to optimize the measurement for such particles [12].

## Muon Spectrometer

The only particles that pass through the calorimeters losing just a little fraction of their energy (they are called minimum-ionizing particles) are the muons. The spectrometer has been designed to provide a muon-trigger in

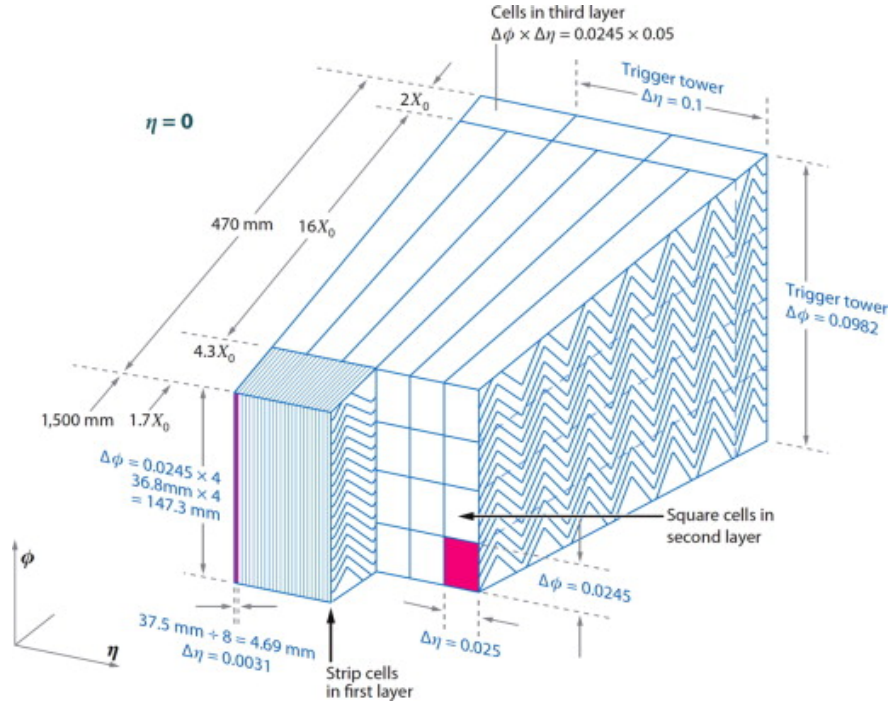


**Figure 1.5** – Overview of a barrel module of the liquid argon electromagnetic calorimeter [12].

the region  $|\eta| < 2.4$  and to measure their momentum in the pseudorapidity range of  $|\eta| < 2.7$ . In the barrel section ( $|\eta| < 1.0$ ) the chambers are settled in cylindrical layers, while in the endcap sections ( $1.0 < |\eta| < 2.7$ ) they are arranged in wheels. The spectrometer defines the overall dimensions of the ATLAS detector. It has a length of 16 m and a diameter of 25 m. It is integrated into the toroidal magnet system that provides a magnetic field of 0.5-1 T within the muon chambers.

An overall view of the MS is shown in figure 1.6. It is composed of two different systems: the trigger chambers and the precision tracking chambers.

The Resistive Plate Chambers (RPC) and Thin Gap Chambers (TGC) are used to provide trigger information, due to their rapid response. The first ones use gas contained in plates spaced by 2 mm. When a particle passes through the RPC, the ionized electrons are multiplied by an electric field and they create a signal read by “ $\eta$  strips”, and by “ $\phi$  strips” which provide the second-coordinate measurement.

The TGC are multi-wire chambers operated in saturated mode, used in the end-cap region for the Level 1 muon trigger (see section 3.2.5). Their anode wires are arranged parallel to the MDT wires and provide position information together with readout strips, which are orthogonal to the wires and are also used to measure the second coordinate.

The chambers for the measurement of the trajectory of the muons are MDT and Cathode Strip Chambers (CSC). Both chambers contain a gaseous mixture which is ionized by the passage of the particle. Through the measurement of the collected electrons it is possible to estimate the trajectory of the muons. The MDT covers the barrel and the end-cap section while the forward region ( $2.0 < |\eta| < 2.7$ ) is covered by the CSC [13].

## Trigger system

The trigger system selects interesting events coming out of the p-p collisions. As it was previously mentioned, the LHC is a high luminosity machine. The average size of an ATLAS event is about 1.3 MB. Multiplying by the LHC average bunch crossing rate of 40 MHz, we get a rather unmanageable data stream of 52 TB/s. To reduce the data stream to a sustainable output of 300 MB/s, corresponding to an event rate of 200 Hz, ATLAS uses a trigger system which provides an on-line selection in three different levels:

the level 1 (L1), the level 2 (L2) and the Event Filter (EF). The first level of trigger is hardware based, it realizes the first selection processing data coming from the muon spectrometer and the calorimeters.



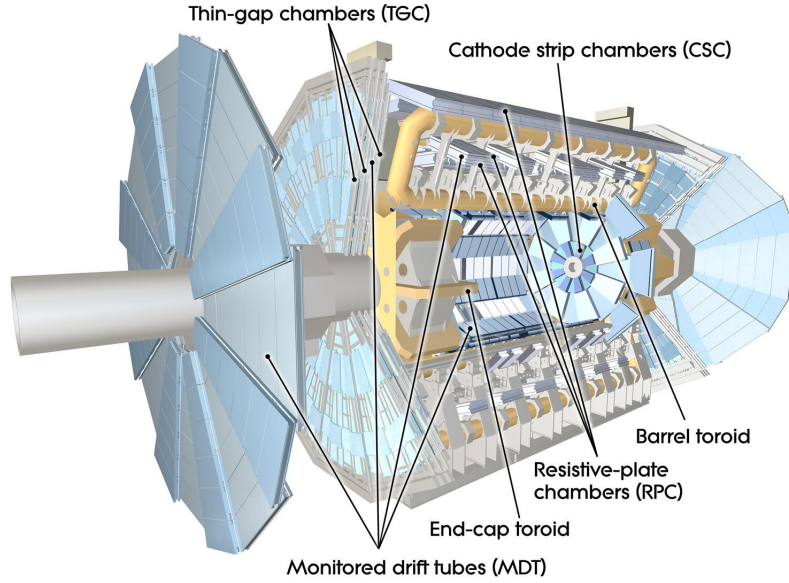


**Figure 1.6** – Artistic illustration of the Muon Spectrometer system and its component [13].

The second level is software based. L2 reduces the trigger rate by 1.5 order of magnitude by combination of events coming from different detectors in order to provide a good precision in the event reconstruction.

The Event Filter is the last step of the on-line selection and it reduces the rate by 1 order of magnitude. Table 1.2 shows the rate and the reduction factors of the above mentioned trigger levels.

	input rate [Hz]	output rate [Hz]	reduction factor
level 1	$4 \times 10^7$	$10^5$	400
level 2	$10^5$	3 000	30
event filter	3000	200	15

**Table 1.2** – The trigger system rates and reduction factors.

## The HL-LHC upgrade

The High Luminosity LHC is a project to increase the luminosity of the Large Hadron Collider by a factor of 5 beyond its design value of  $\mathcal{L} = 10^{34} \text{cm}^{-2} \text{s}^{-1}$  by  $\sim 2025$ . Compared to the Large Hadron Collider (LHC), the High Luminosity LHC will provide accurate measurements of the Higgs couplings and enable observation of rare processes beyond the actual sensitivity levels. The project relies on a number of key innovative technologies for upgrading the LHC, such as cutting-edge 12 T superconducting magnets with large aperture, compact and ultra-precise superconducting cavities for beam rotation, new types of collimators and high-power superconducting links with almost zero energy dissipation [1].

At the end of the current LHC programme the ATLAS detector will be running with components that are 15-20 years old. In particular, the silicon tracking systems will be approaching the end of their lifetimes:  $700 \text{fb}^{-1}$  for the strip system and  $400 \text{fb}^{-1}$  for the pixel system. Moreover, the higher luminosity will increase significantly the occupancies in both the silicon detectors, and the occupancy in the straw tube transition radiation tracker (TRT) will reach  $\sim 100 \%$ , severely compromising the tracking performance.. The need for good performance in vertex and track reconstruction, even in the high occupancy and radiation fluence environment of the HL-LHC, require a complete replacement of the current tracking system. Therefore, a new

---

all-silicon tracker (ITk) must be installed. The choice of sensors depends on the requirements that the detector has to withstand an expected fluence of  $3000\text{ fb}^{-1}$ . The innermost layer will be exposed to an estimated fluence of  $1.4 \times 10^{16}\text{ n}_{eq}/\text{cm}^2$ . For the outer pixels, the expected maximum fluence is  $1.7 \times 10^{15}\text{ n}_{eq}/\text{cm}^2$  [1]. New radiation-hardness particle detectors, based on the commercial well-established High-Voltage CMOS (HV-CMOS) technology, have been proposed for the ITk. In the following I will describe in more detail the operating principle of such a technology.

### 2.1 Interactions of charged particles with matter

Charged particles moving through matter interact with the electrons in the material. The mean energy loss due to ionization (also called stopping power) is given by the Bethe-Bloch formula [14]:

$$\left\langle -\frac{dE}{dx} \right\rangle \frac{1}{\rho} = K z^2 \frac{Z}{A} \Phi(\beta)(1 + \nu) \quad (2.1)$$

$$\Phi(\beta) = \frac{1}{\beta^2} \left( \frac{1}{2} \ln \frac{2m_e c^2 \beta^2 \gamma^2 T_{max}}{I^2} - \beta^2 - \frac{\delta}{2} \right) \quad (2.2)$$

Where:

- $\frac{dE}{dx}$ : energy loss of the particle in units of  $\frac{MeV}{g/cm^2}$
- $K=4\pi N_A r_e^2 m_e c^2 = 0.307075 \text{ MeV cm}^2$
- $z$ : charge of the traversing particle
- $Z$ : atomic number of the absorbing medium (14 for silicon)
- $A$ : atomic mass of the absorbing medium (28 for silicon)
- $\rho$ : mass density of the absorbing medium [ $g/cm^3$ ]
- $m_e c^2$ : rest energy of electron (0.511 MeV)
- $\delta$ : density correction due to the polarization of the atoms by the electric field of the traversing particle
- $\beta = v/c$ : velocity of the traversing particle and  $\gamma = \frac{1}{\sqrt{1-\beta^2}}$
- $I$ : mean excitation energy (137 eV for silicon)
- $T_{max}$ : maximum energy transfer possible in a single collision
- $\nu$ : higher order correction  $\mathcal{O}(z^3, z^4, \dots)$

Formula 2.1 results from a calculation to the lowest non-vanishing order of the Born approximation of the interaction between the incident particle and the atomic electrons. It describes the mean rate of energy loss per unit length in the region  $0.1 \lesssim \beta\gamma \lesssim 0.01$  for intermediate  $Z$  materials with an accuracy of few %. At low energy of the traversing particle (for copper  $\beta\gamma \sim 0.3$ ), i.e. at particle velocities comparable to those of outer atomic electrons, higher-order corrections become significant, these are the *Bloch* correction ( $\mathcal{O}(z^4)$ ) and the *Barkas* correction ( $\mathcal{O}(z^3)$ ) which differentiate between positive and negative charge of the traversing particle. At high energies (for copper  $\beta\gamma \sim 100$ ) radiative corrections which result from the multiple virtual emission of photons by the incident particle become significant; at even higher energy ( $\beta\gamma \sim 1000$ ) they represent the dominant process in the energy loss mechanism.

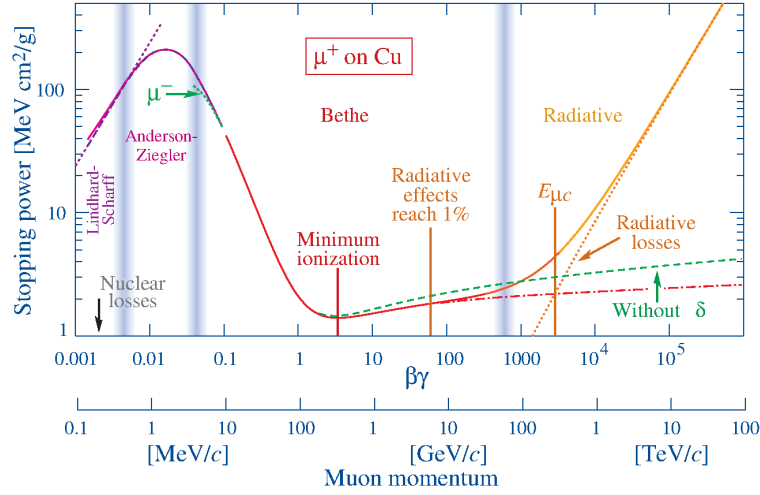


**Figure 2.1** – Stopping power for a muon in copper as a function of  $\beta\gamma = p/Mc$  [15].

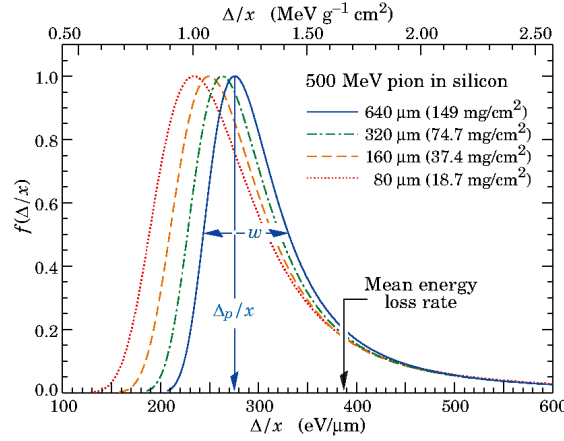


**Figure 2.2** – Landau distribution for different thickness of the detector [15].

As shown in figure 2.1 the stopping power functions are characterized by a broad minima. In most practical cases the incident particles have a mean energy loss close to this minima. They are called minimum-ionizing particles or briefly ”*mip*” [15].

The energy loss of a particle passing through matter is subject to statistical fluctuations. For a sensor of moderate thickness<sup>1</sup> the energy loss probability distribution is described by the Landau-Vavilov distribution [17, 18]. The Bethe-Bloch equation describes the mean of such a distribution. However because of its long tail the mean differs from the most-probable value. The latter can be expressed as:

$$\Delta_p = \xi \left[ \ln \frac{2mc^2\beta^2\gamma^2}{I} + \ln \frac{\xi}{I} + j + \beta^2 - \delta \right] \quad (2.3)$$

where  $\xi = K/2 \langle Z/A \rangle x / \beta^2$  for a detector with a thickness  $x$ ,  $j = 0.20$  is a unitless constant [19]. The Landau-Vavilov distribution is shown in figure 2.2 for different thicknesses of the material. The tail of the distribution is due to the so called  $\delta$ -electrons. They are formed when the incident particle transfers enough energy such that the electrons themselves produce secondary ionization. In reality, because of the finite energy resolution of the detector, the collected electrons distribution is a convolution of a Landau-Vavilov and a Gaussian.

1. Formally this is related to the mean number of collisions, see [16] for details.



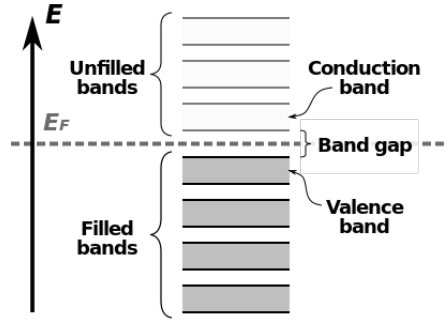


**Figure 2.3** – Semiconductor band structure at zero temperature where no thermal excitation is present. The valence band is the last filled energy range and the conduction band is the first unfilled energy range. The band-gap is the difference between the two bands, in this region no free carriers are present. The Fermi energy  $E_F$  (see text) is located in the middle of the band-gap.

## 2.2 Semiconductor properties

Semiconductor detectors have a broad field of applications during the last decades for  $\gamma$  and X-ray spectrometry and as particle detectors. The first experiments which used a silicon-based tracker were the CERN's NA11 and NA32 [20]. Since then silicon detectors have been widely used in high energy physics experiments. In the following, the main properties of silicon for particle detection are discussed.

The periodic structure of the crystal lattice allows to describe the electrons of the silicon atoms, in the energy-impulsion domain, in a band structure with forbidden zones where an electron cannot be found, the so called band-gap. The valence band is defined as the highest accessible electron energy range at absolute zero temperature. Similarly, the conduction band is the lowest unfilled band at 0 K as shown in figure 2.3. If an electron in the valence band acquires an energy greater than the height of the band-gap, it can pass to the conduction band where it is free to move through the lattice. In the case of a particle detector this energy is released by the traversing particle through ionization (see previous section).

The band-gap in silicon is 1.12 eV [19]. Thus the number of electron-hole (e-h) generated by a traversing particle is calculated by dividing the deposited energy ( $E$ ) by the mean energy needed for ionization ( $\epsilon$ ):  $N_{e-h} = \frac{E}{\epsilon}$ , where  $\epsilon = 3.6$  eV. The energy required to create an electron-hole pair is bigger than the band gap because silicon is an indirect semiconductor<sup>2</sup> and therefore some energy is lost in vibrations of the lattice.

The energy distribution of the free carriers is described by the Fermi-Dirac distribution :

$$n_i = \frac{g_i}{1 + e^{\frac{E_i - \mu}{k_B \cdot T}}} \quad (2.4)$$

where  $g_i$  is the degeneracy factor of the energy state and  $\mu$  is the Fermi-Dirac quasi-energy. The Fermi energy  $E_f = \mu(T = 0)$  is the highest occupied energy level.

It is possible to implant impurities in the device in order to change its electrical properties. These are atoms from the third and fifth group, usually boron and phosphorus. The latter, called donors, introduce valence electrons. The former, called acceptor, introduce a lack of an electron at a position where one could exist in an atom or atomic lattice, this lack can be formally expressed as a virtual particle with positive charge and it is called a hole [21]. It can be shown that the Fermi energy shifts towards the conduction band when a concentration of donor atoms  $N_D$  is present. This fact implies an increase of the electron concentration ( $n$ ) which is followed by a decrease of the hole concentration ( $p$ ) according to the mass action law  $n_i^2 = np$ , where  $n_i$  is the carrier concentration of the undoped silicon (also called intrinsic concentration). Silicon doped with donors is called *n-material*. Similarly, for acceptors the Fermi energy shifts towards the valence band increasing the hole concentration and silicon doped with acceptors is thus called *p-material*.

2. The minimal-energy state in the conduction band and the maximal-energy state in the valence band are characterized by different value of the momentum. Therefore a transition between the valence and the conduction band is only possible via phonon exchange.

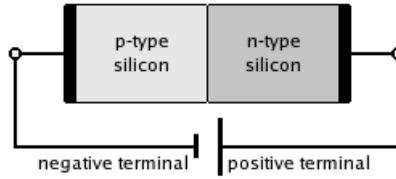


**Figure 2.4** – A reversed biased diode.

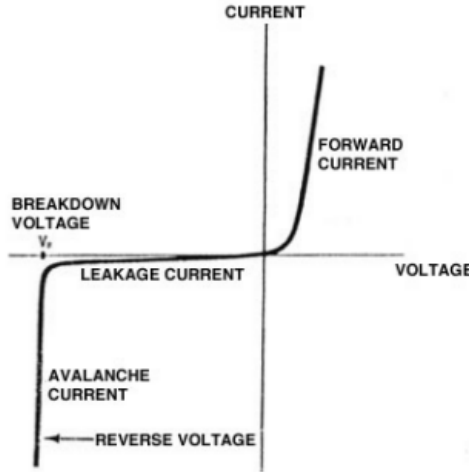


**Figure 2.5** – A typical diode IV characteristic. Three main region are present as a function of the applied voltage. If the polarity of the external voltage opposes the built-in potential ( $\sim 0.3$  V) an electric current through the pn-junction is observed (forward current). For negative bias voltage the depletion region acts as an insulator, however charge carriers can be thermally activated contributing the so-called leakage current. When the reverse bias voltage exceeds the breakdown voltage, an abrupt increment of the reverse current is observed.

## 2.3 The pn-junction

When a p-doped semiconductor and a n-doped one are put into contact, a pn-junction is formed. Because of the concentration difference of the free charge carriers, the majority carriers from one side diffuse into the other doped side. Holes and electrons recombine creating a region which is depleted from the free charge carriers, the so-called depletion zone. Due to the acceptor and donor ions this region, is electrically charged. The remaining electric field (refereed as built-in electric field) counteracts the diffusion so that an equilibrium is reached.

When an external voltage is applied in such a way that the negative terminal is connected to the p-material as shown in figure 2.4, the holes and electrons are pulled away from the depletion zone. In such conditions the junction is reversely biased and the width of the depletion increases. The typical IV characteristic for a diode is shown in figure 2.5.

Solving the Poisson equation under the assumption that donors and acceptors are completely ionized one finds [19]:

$$W(V) = x_p + x_n = \sqrt{\frac{\epsilon_0 \epsilon_{Si}}{e} \left( \frac{1}{N_A} + \frac{1}{N_D} \right) (V + V_{bi})} \quad (2.5)$$

where:

- $W$  is the width of the depletion zone
- $N_A$  and  $N_D$  are the acceptor and donor concentrations. These values are linked to the resistivity of the material through the relation:  $\rho = \frac{1}{q(\mu_n n + \mu_p p)}$  where  $\rho$  is the resistivity,  $\mu_n/p$  the electrons and holes mobility. In the case of heavily doped material  $N_{A(D)} \approx p(n)$  and the previous equation can be simplified as:  $d \propto \sqrt{\rho V}$
- $V_{bi}$  is the built-in voltage and represents the voltage which is intrinsically formed at the pn-junction .

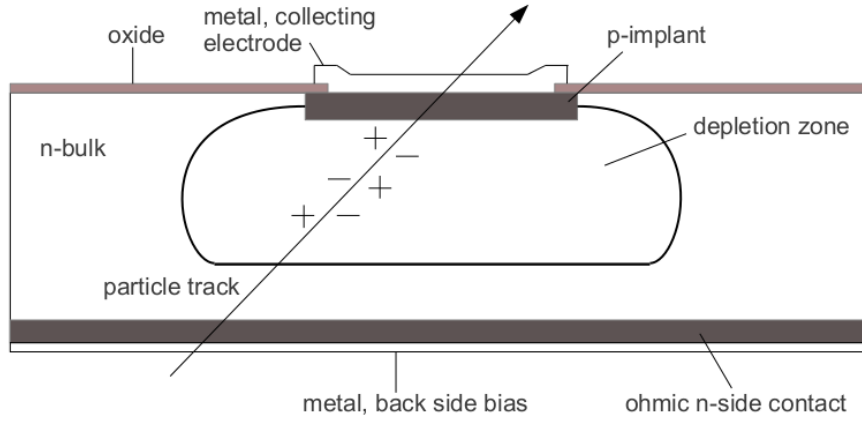


**Figure 2.6** – Schematic cross section of a pixel detector. In this example the pn-junction is formed by an n-doped substrate and a heavy p-doped layer (typically  $\sim 10^{19} \text{ cm}^{-3}$ ). The generated signal is collected by the collecting electrode. The bias voltage is applied at the backside metal contact. An heavy n-doped layer is needed to form a ohmic contact with the metal avoiding a direct metal-semiconductor contact (Schottky diode). The oxide is needed to insulate the silicon.

Because of the absence of free charges in the depletion zone, the e-h pairs created by the interaction of a traversing particle can be easily collected. A pixel sensor is in fact a reversely biased pn-diode with a highly segmented cathode or anode. Equation 2.5 shows that by increasing the applied voltage ( $V$ ) and the resistivity ( $\rho$ ) of the silicon, the size of the depleted region increases, thus the amount of collected charge increases and therefore an improvement of the performance of the detector such as efficiency and timing is expected. Figure 2.6 shows a schematic cross section of single pixel detector.

### Signal formation

The instantaneous charge  $Q$  induced at the collecting electrode by the movement of the charge carriers is given by the Shockley–Ramo theorem [22]:

$$Q_k = \sum_{n=1} q_i \phi_k(r_{i_f}^{\vec{r}}) - \sum_{n=1} q_i \phi_k(r_{i_0}^{\vec{r}}) \quad (2.6)$$

Where  $r_{i_0}^{\vec{r}}$  and  $r_{i_f}^{\vec{r}}$  are respectively the initial and final position of the carrier,  $\phi_k(r_{i_f}^{\vec{r}})$  is the "weighting potential" (also called *Ramo* potential) obtained by raising the electrode under consideration to unit potential, setting all others to zero, and solving the Poisson equation [19]. The theorem is based on the concept that current induced in the electrode is due to the instantaneous change of electrostatic flux lines which end on the electrode, not the amount of charge received by the electrode per second. Integrating the previous equation one gets:  $i = qE_w v$ , where  $v$  is its instantaneous velocity of the carriers and  $E_w$  the component of the "weighting electric field" in the direction of  $v$ . It is therefore important to discuss the transport mechanism of free carriers in silicon to understand how it influences the collected signal.

### Charge transport

Two main effects characterize the charge transport: the diffusion and the drift.

The first one is characterized by the random thermal motion of free carriers which implies a net movement from a high concentration region to a low concentration one. This effect can be quantified by the following relations:

$$J_{n,\text{diff}} = -D_n \nabla n \quad ; \quad J_{p,\text{diff}} = D_p \nabla p \quad (2.7)$$

where  $J_{n/p,\text{diff}}$  is the diffusive current density,  $n$  and  $p$  are the electron and hole concentration respectively and  $D_{n/p}$  the diffusion constant related to the mobilities via the Einstein relation  $D_{n/p} = \mu_{n/p} kT/e$ .

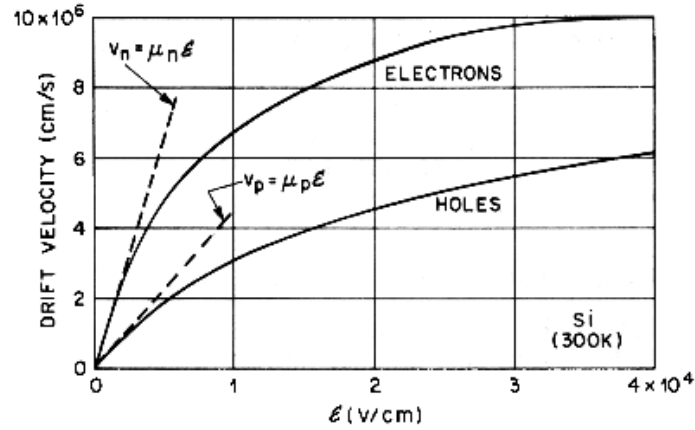


**Figure 2.7** – Electrons and holes drift velocity as a function of the electric field [19].

The drift component is described by the Drude model. According to this model a charge carrier in the presence of an electric field is accelerated between two random collisions. The direction is driven by the field leading to an average drift velocity given by:

$$v_n = -\mu_n E \quad ; \quad v_p = -\mu_p E \quad (2.8)$$

where the mobility is defined as  $\mu_{n/p} = \frac{q\tau_{n/p}}{m_{n/p}^*}$  with  $\tau_{n/p}$  being the characteristic time between two collisions and  $m_{n/p}^*$  the effective mass [21] of the electrons and holes respectively. This relation however does not hold for higher value of the electric field when the acquired velocity is comparable to the thermal velocity of the carriers ( $\sim 10^5 m/s$ ). As the acceleration increases, the number of collisions becomes higher leading to a saturation of the drift velocity (figure 2.7). This effect is also known as "mobility degradation". In this condition the mobility can be parametrised using the following relation [19]

$$\mu(E) = \mu_0 \frac{1}{[1 + (\frac{\mu_0 E}{v_{sat}})^\beta]^{\frac{1}{\beta}}} \quad (2.9)$$

where the different parameters are shown in table 2.1. The drift current per unit area is defined as:  $J_{n(p),\text{drift}} = \mu_{n(p)} q n(p) E$  where  $E$  is the electric field. The total carrier density is therefore  $J_{n(p)} = J_{n(p),\text{drift}} + J_{n(p),\text{diff}}$ . In chapter 4 and 5 the effect of both the drift and diffusion component on the induced signal of the detector is studied in details using test-beam data and simulations.

	Electrons	Holes	Unit
$\mu_0$	1417	470.5	$cm^2/Vs$
$\beta$	2.0	1.0	unitless
$v$	$1.07 \times 10^7$	$8.37 \times 10^6$	$cm/s$

**Table 2.1** – Parameters to describe the mobility of electrons and holes (see eq. 3.9). Values are for T=300 K [23].

## Generation-Recombination

The transfer of electrons from the valence band to the conduction band is referred to as the generation of electron-hole pairs (or pair-generation process). The inverse process is termed recombination. Once that free carriers have been generated, they can eventually recombine in the bulk of the device. This recombination

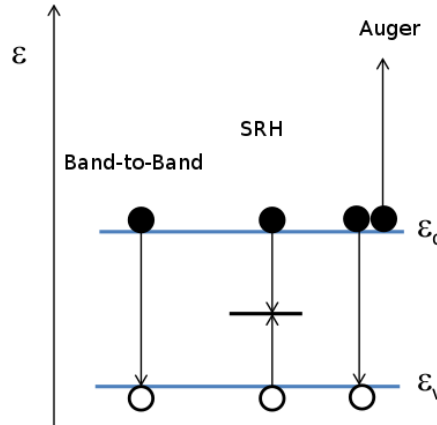


**Figure 2.8** – Generation/Recombination models in silicon.

mechanism decreases the amount of collected charge and therefore decreases the induced signal at the electrode. On the contrary, if by thermal excitation an electron-hole pair is formed, it will generate a noise signal in the collecting electrode.

Three main models characterize the generation-recombination processes (see figure 2.8):

- Direct recombination (or band-to-band recombination): Electron in the conduction band releases energy and recombines with hole in the valence band.
- Indirect recombination: Carriers recombine via trap states in the forbidden gap, for indirect semiconductors it is described by the Shockley-Read-Hall (SRH) process. These centers are created by defects of the crystal lattice (see next section).
- Auger recombination: The energy released from the recombination is given to a third carrier which is excited to a higher energy level without moving to another energy band.

Energy transitions via intermediate trap levels are energetically favoured over band-to-band transition, and recombination through shallow traps can occur without phonon exchange. Therefore, in indirect semiconductors as silicon, the SRH model is the most important generation-recombination mechanism among those mentioned above.

## 2.4 The SRH model

There are four processes which characterize the SRH model: two recombination mechanisms which release energy and two generation mechanisms which need energy to occur (see figure 2.9). The recombination rate is expressed by the following formula [24]:

$$R_{SRH} = \frac{(np - p^2)}{\tau_n(n + n_t) + \tau_p(p + p_t)} \quad (2.10)$$

where  $n_t$  ( $p_t$ ) is the concentration of trapped electrons (holes) and  $\tau_{n/p}$  represents the recombination lifetimes, depending mostly by the purity of the silicon they are described as a function of the doping by the Scharfetter relation [23]:

$$\tau_{dop} = \frac{\tau_{n/p}}{1 + \left(\frac{N_A + N_D}{N_{ref}}\right)^\gamma} \quad (2.11)$$

Where the parameters are summarized in table 2.2. It is worthwhile to say that a high resistivity not only increases the depletion region but it also increases the recombination lifetime resulting in a low recombination rate.

	Electrons	Holes	Unit
$\tau_{n/p}$	$1 \times 10^{-5}$	$3 \times 10^{-6}$	s
$N_{ref}$	$1 \times 10^{16}$	$1 \times 10^{16}$	$cm^{-3}$

**Table 2.2** – Parameters to describe the Scharfetter relation [23].

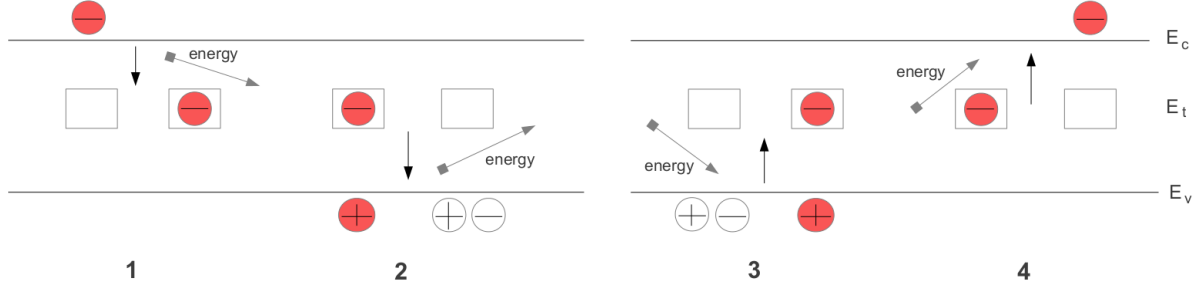


**Figure 2.9** – Generation/Recombination through shallow trap. Regarding the recombination: 1) an electron in the valence band can be captured by the impurity releasing an amount of energy of  $\sim E_c - E_t$ . 2) an electron from the trap state can pass to the valence band and then recombine with a hole releasing a energy of  $\sim E_t - E_v$ . For the generation mechanism: 3) an electron excited with an energy  $\sim E_v - E_t$  can pass from the valence band to the trap so that an hole is formed. 4) an electron from the trap level can be excited with an energy  $\sim E_c - E_t$  to the conductance band.

## 2.5 Radiation damage in silicon devices

The energy loss in silicon detectors can be split into Non-Ionizing Energy Loss (NIEL) and in Ionizing Energy Loss. The former displaces crystal atoms forming defects in the crystal lattice. They change the electric properties of the Silicon by introducing energy levels in the forbidden band-gap. Through these defects electrons in the conduction band or holes in valence band can be trapped and eventually recombine as discussed in the previous section. Despite ionization is the main mechanism for energy loss of charged particles in matter, hadrons can collide with the atoms of the lattice through strong interaction. NIEL is defined as the amount of energy released into the material by an incident particle which is not due to ionization. Different particles have different effectiveness in releasing NIEL, therefore the irradiation damage is normalized to the NIEL of a 1 MeV neutron. The induced defects can drastically change the macroscopic properties of the material, the main effects due to the NIEL are:

- Space charge sign inversion
- Modification of full depletion potential
- Increase of the leakage current

As radiation induces electrically active defects, the doping of the material is altered. Due to a donor removal mechanism, the doping concentration changes with the irradiation. It is thus useful to define an effective doping concentration  $N_{eff}$  which is the difference between all donor-like states and all acceptor-like states. Due to the fact that  $N_{eff}$  changes with the fluence, thus affecting the depletion region, usually the bias voltage must be increased along the lifetime of the experiment.  $N_{eff}$  can be determined by inverting equation 3.5:

$$|N_{eff}| = \frac{2\epsilon_0\epsilon_{Si}V_{depl}}{et^2} \quad (2.12)$$

where  $V_{depl}$  is the bias voltage needed to reach full depletion and  $t$  is the thickness of the sensor. It has been shown that starting from an n-doped material  $N_{eff}$  decreases until it changes sign as it is dominated by the acceptor-like defects as shown in figure 2.10. This mechanism is known as *space charge sign inversion*. The defects and their reactions are not understood in details, a phenomenological parametrization has been performed and the corresponding model is called the *Hamburg model* [25].

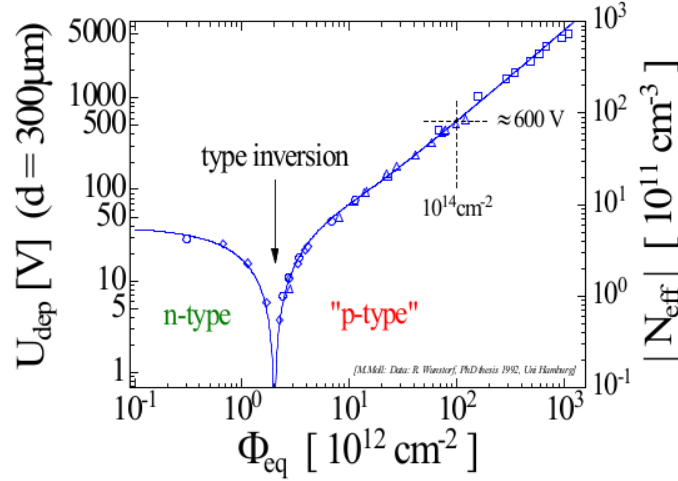


**Figure 2.10** – Change of the full depletion voltage of a 300  $\mu\text{m}$ -thick silicon sensor and its absolute doping versus the normalized fluence [26].

Since the traps act as generation-recombination centers (see previous section) the thermal activation of an electron-hole pair is more frequent, therefore the generation lifetime  $\tau_g$ <sup>3</sup> decreases resulting in an increase of the leakage current density in the bulk. Its variation can be parametrised as follows [25] :

$$\Delta J = \alpha \phi \quad (2.13)$$

with  $J$  being the leakage current density and  $\alpha$  the *current related damage rate* which depends on the initial resistivity of the silicon. The leakage current increases linearly with the fluence  $\phi$  as shown in figure 2.11. This effect can be mitigated by cooling down the sensor so that the thermal activation through shallow traps is reduced.

In contrast to the NIEL which affects the bulk of the device, the ionizing energy loss affects mostly the silicon-dielectric interface (see figure 2.6). The dose of ionizing energy loss radiation damage is usually expressed in Rad, which represents  $6.24 \times 10^{10} \text{ MeV}$  of ionizing energy deposition per kilogram of material. An ionizing particle creates electron-hole pairs in the oxide. Since the electrons have high mobility in the oxide ( $\mu_{n,oxide} = 20 \text{ cm}^2/(\text{Vs})$ ) they are quickly collected. The holes instead have a very low mobility ( $\mu_{p,oxide} = 2 \times 10^{-5} \text{ cm}^2/(\text{Vs})$  [19]) because of the large number of shallow traps in the oxide. They tunnel from one trap to the other in the direction of the electric fields until they reach the oxide/silicon interface where a large number of deep hole traps exist [19]. This positive charged layer in the  $\text{SiO}_2$  attracts free electron carriers in the bulk; in the case of p-doped silicon an inversion layer is formed which can eventually short two neighboring n-doped pixels implant. In order to avoid this effect, three techniques have been developed: an heavy p-doped region can be implanted in between the implants (*p – stop*). Alternatively one can form a light p-doped region which extends up to the all inter-pixel length (*p – spray*). Furthermore a combination of the two methods can be implemented [19]. A detailed discussion on this topic is out of the scope of this thesis, but the effect of the p-implant on the properties of device in analysis is shown in details in chapter 5.

3. characteristic time between two thermally excited pairs creation.

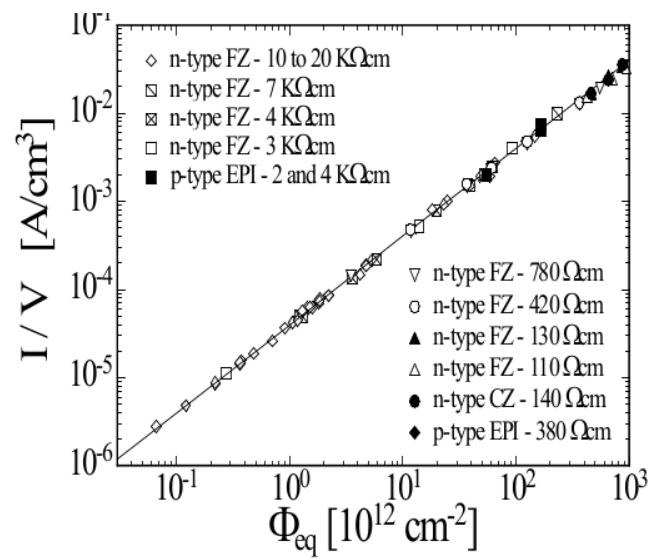


**Figure 2.11** – Current related damage rate fitted with experimental data [25].



---

The HV-CMOS pixel technology

---

The High-Voltage CMOS (Complementary Metal Oxide Semiconductor) technology was originally used to design the electronic chips that drive automotive or industrial devices. It is suited for a wide variety of applications including smart sensors, sensor interface devices, building controls and LED lighting control. They have also been proposed as particle detectors [27]. Such devices contain simple circuits, e.g. amplifiers and discriminators, but still require a traditional (pixel or strip) readout chip. In our study the HV-CMOS device and a FEI4 chip are glued onto the sensor so that the sensor electrodes and the input pads of the readout channels form capacitors. This assembly is called Capacitively Coupled Pixel Detector (CCPD).

### 3.1 The FE-I4 chip

The extreme operating condition of the IBL (see chapter 1, section 3) have necessitated the development of new front-end read-out chip, called the FE-I4. The FE-I4 consists of an array of 26,880 pixels, 80 in the z-direction (beam direction) and 336 in the azimuthal  $r\phi$  direction (referring to the ATLAS detector coordinates, chapter 1). The pixel size is  $250 \times 50 \mu m^2$ .

The FE-I4 has a pixel matrix architecture that is different from the previous read-out chip, the FE-I3 (used in the ATLAS pixel detector) which is characterized by a pixel column drain readout followed by peripheral data storage and trigger logic. Figure 3.1 shows the two read-out chips. For the FE-I4 the data storage is made locally at the pixel level until triggering and subsequent propagation of the trigger inside the pixel array.

Each pixel consists of an independent analog section, amplifying the collected charge from the sensor. In the analog section, hits are discriminated at the level of a tunable comparator with an adjustable threshold, and charge is translated to Time over Threshold (ToT). The 26,880 pixel array is organized in columns of analog pixels, each pair of analog columns tied to a shared digital double-column unit centered between them. Inside the double-column, 4 analog pixels communicate to a single digital region as shown in figure 3.2. When a trigger confirms a hit, ToT buffers are sent to the periphery and associated to the bunch-crossing corresponding to the specific trigger. More technical details can be found elsewhere [9].

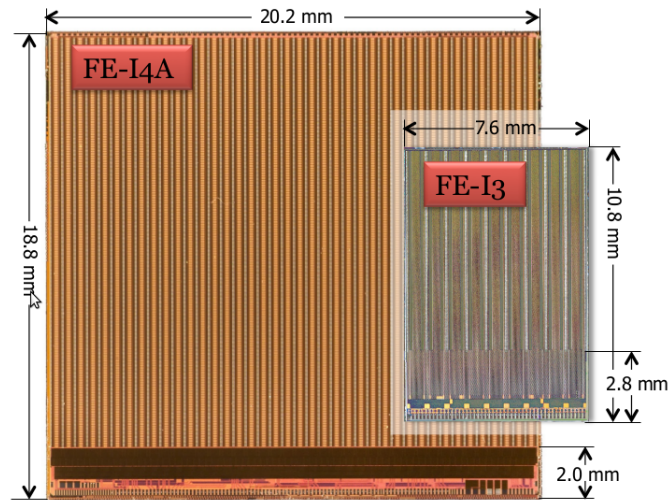


**Figure 3.1** – Picture of the FE-I4A IC and the FE-I3 (previous read-out chip) [9].

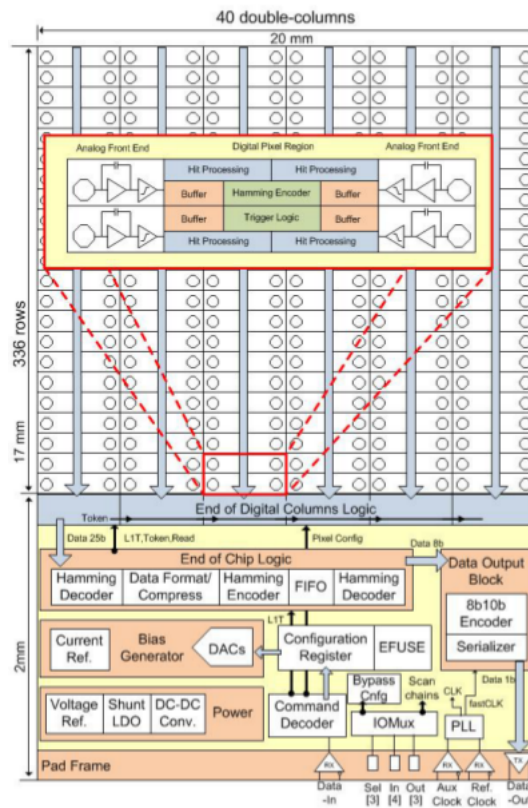


**Figure 3.2** – Block-diagram of the FE-I4 read-out chip [9].

### 3.2 The HV-CMOS pixel technology

The HV-CMOS technology allows to combine the standard submicron-size CMOS transistors that typically operate at 3.3 V and larger specially shaped transistors that are able to handle high-voltage signals ( $\sim 100$  V). The low-voltage transistors are used to implement the internal electronics of the chip and the high-voltage devices are used in the output drivers [27].

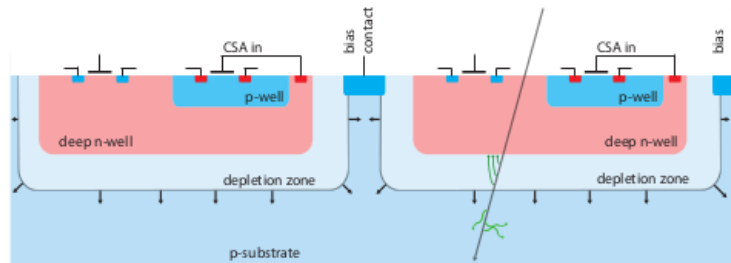


**Figure 3.3** – Simplified cross section of an HV-CMOS sensor. A reverse bias is applied at the top of the device. The deep n-well plays two roles: it is the signal collecting electrode and the substrate for the NMOS transistors. A ionizing particle deposits energy in the thin depletion zone and creates electron-hole pairs which are collected by drift or diffusion [28].

The operating principle of the HV-CMOS is described in figure 3.3. A deep n-well is implanted in a low resistivity p-type substrate ( $\sim 20 \Omega\text{cm}$ ) and it acts as the signal collecting electrode. Read-out circuitry is placed in the deep n-well which contains a p-well in order to use both NMOS and PMOS transistors. The deep n-well provides isolation for the low-voltage devices from the p-type substrate so that it can be biased with a high-voltage. As the deep n-well it is the collecting electrode and the substrate of the transistors, such a device is referred to as "smart" diode and the pixel array is a "smart diode array" (SDA).

As already mentioned, the FE-I4 readout chip is glued onto the sensor so that the sensor electrodes and the input pads of the readout channels form capacitors. In this way, the voltage signals can be transmitted from the sensor to the readout chip by means of AC coupling. This assembly yields to the following benefits:

- With a substrate resistivity of about  $20 \Omega\text{cm}$  and a bias voltage of 60 V, the depletion zone extends around  $15 \mu\text{m}$  into the substrate. The expected charge collected by drift is therefore in the order of 1000 electrons. This relatively low signal can still be detected and amplified thanks to the on-chip electronics.
- On-chip signal amplification makes it possible to use AC-coupling to the readout chip. Instead of the expensive bump-bonding, the sensor chip can be simply glued to the FE-I4 chip.
- Since the charge collection occurs approximately at the surface, thinning of the detector is possible down to  $\sim 50 \mu\text{m}$ .
- The pixel size can be made smaller because no bump-bonding is needed. Smaller pixel size leads to smaller input capacitance, better position resolution and higher granularity. The latter is particularly significant for the HL-LHC because of the high pile-up environment.
- The HV-CMOS process is a standard electronic production process and therefore cheap and widely available.
- The thin depletion zone allows for a very fast charge collection that in turn leads to low sensitivity to charge trapping at lattice defects. Since charge trapping is the main reason for sensor degradation by non-ionizing radiation, a high bulk radiation hardness can therefore be expected. In addition deep sub-micron CMOS technology is designed to be resistant to ionizing radiation so high radiation hardness of the electronics is also expected [29].

These properties make the HV-CMOS technology a suitable candidate for the pixel sensor of the inner detector of the ATLAS experiment for the HL-LHC.

## The Devices Under Test

The prototypes investigated in this project were produced by the Austria MicroSystems (AMS) 180 nm high-voltage process. The bare HV-CMOS sensor is connected to a FE-I4 by precision gluing protocol, the epoxy glue used is approximately  $3\text{ }\mu\text{m}$  thick. Both the HV-CMOS sensor and the FE-I4 chip are wire-bonded to a PCB (Printed Circuit Board) as shown in figure 3.4 [27]. A typical IV-curve of a CCPD is shown in figure 3.5. During this work CCPD version 2 (v2) and 4 (v4) have been analyzed in test-beam and the upcoming demonstrator prototype has been simulated using TCAD tools.

- **CCPDv2:** An overall view of the HV-CMOS sensor is shown in figure 3.6(a). The pixel matrix is composed of three different pixel flavors. "Rad-hard" pixels, "Simple" pixels<sup>1</sup> and "standard" pixels. The entire matrix consists in  $20 \times 12$  unit cells with a single pixel dimensions of  $125 \times 33\text{ }\mu\text{m}^2$ . The pixel electronics are based on a charge-sensitive amplifier and a comparator. The sensors were adapted to FE-I4 readout chip. As the FE-I4 pixel dimensions are larger than the HV-CMOS pixel, three HV-CMOS pixels are connected to a single FE-I4 pixel as shown in figure 3.7(a). Output stages of the sub-pixels are globally adjustable allowing an encoding of the hit position.
- **CCPDv4:** The single pixel structure is similar to the v2, the in-pixel electronics is made of a charge-sensitive amplifier and a comparator. the CCPDv4 pixels matrix is composed of four different pixels flavors as shown in figure 3.6(b) and 3.7(b). The STime, the Samps, the Analog pixels and the "new-pixels". The STime and Samps pixels have dimensions of  $125 \times 33\text{ }\mu\text{m}^2$  but they present a different sub-pixel encoding procedure. The first one relies on the length of the output signal of the comparator (STime) while the latter uses its amplitude (Samps). The Analog pixels have a different dimensions w.r.t. the previous ones:  $250 \times 25\text{ }\mu\text{m}^2$ . In order to analyze the output of the pre-amplifier, They do not have a comparator in the in-pixel electronics. In addition to these flavors there are the so called "new-pixels" which have not been tuned and therefore not analyzed.
- **Upcoming demonstrator:** A full-size HV-CMOS prototype is foreseen for September 2015. The ITk requirements demand high efficiency ( $\sim 99\%$ ) in 2 b.c. (50 ns). In order to fulfill these conditions and exploit in detail the properties of the HV-CMOS technology, the new demonstrator has been designed with different pixel types: two CCPD pixel flavors divided into digital pixels (the in-pixel electronics is formed by a pre-amplifier and a discriminator) and analog pixels (pre-amplifier only), and standalone pixels (they are not coupled to an FE-I4 pixel, they contain a pre-amplifier and a discriminator as well as read-out architecture in the periphery). All the pixel flavors will be implemented with different rise times of the pre-amplifier (low, fast, and the so-called super-fast). Also the pixel dimensions will change:  $250 \times 50\text{ }\mu\text{m}^2$  matching the FE-I4 1-to-1. Furthermore, four different HV-CMOS substrate resistivities are expected:  $20\text{ }\Omega\text{cm}$ ,  $80\text{ }\Omega\text{cm}$ ,  $200\text{ }\Omega\text{cm}$  and  $1000\text{ }\Omega\text{cm}$ . The three pixel flavors have a common HV-CMOS pixel structure. Such a structure has been studied using TCAD simulations as discussed in detail in the chapter 5.

1. The "Rad-hard" pixels present enclosed transistors and guard rings. The "Simple" pixels present a simplified circuitry compared to the other p flavors. During test-beams these pixel flavors have not been tuned.

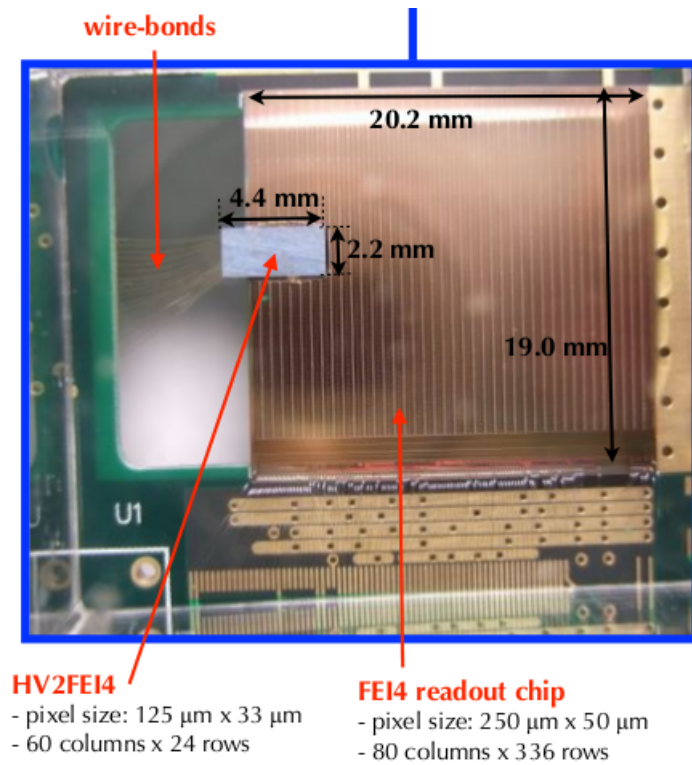


**Figure 3.4** – Picture of an HVCMOS sample glued to an FEI4 and wire-bonded to a PCB.

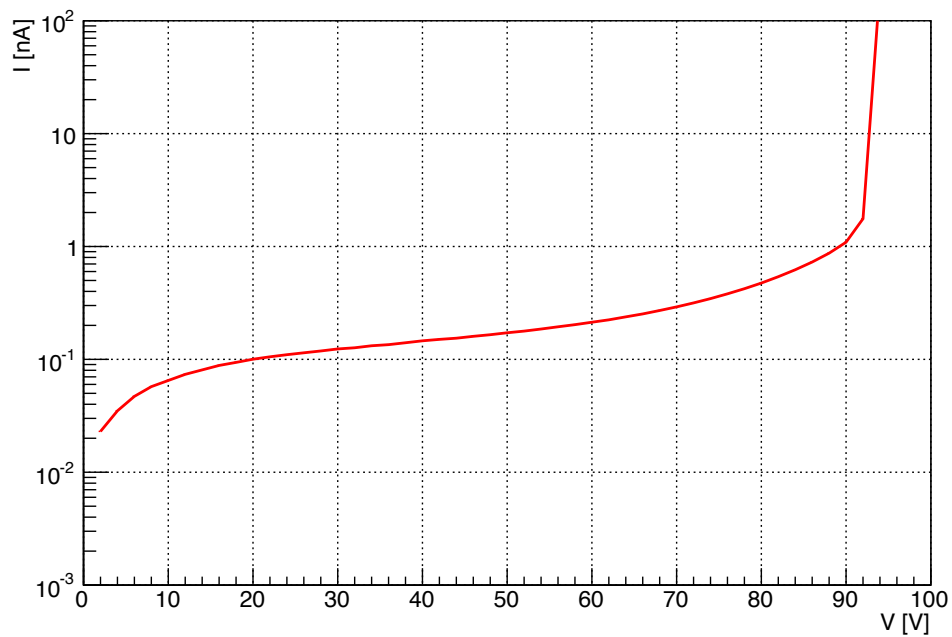


**Figure 3.5** – IV curve of a CCPD. A negative bias voltage is applied. The breakdown voltage is at  $\sim 93\ \text{V}$ .

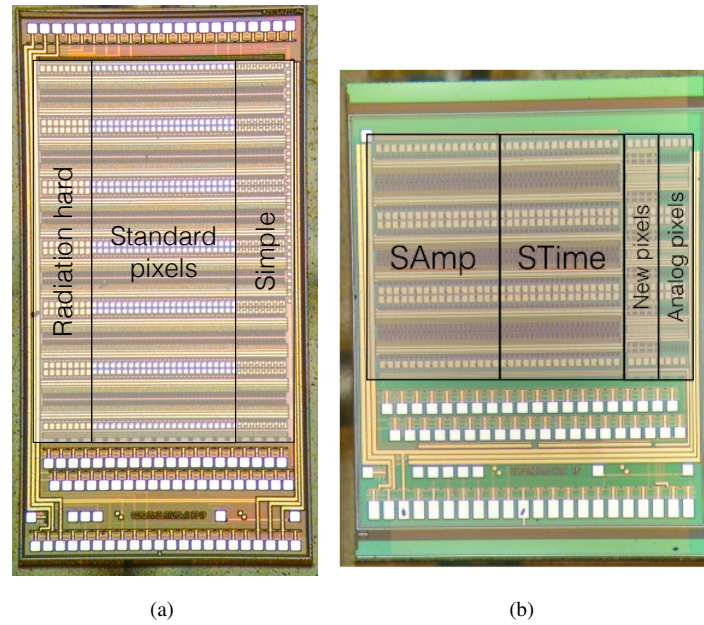


**Figure 3.6** – Bare HV-CMOS sensors with different pixel types. a) version 2. b) version 4 [30].

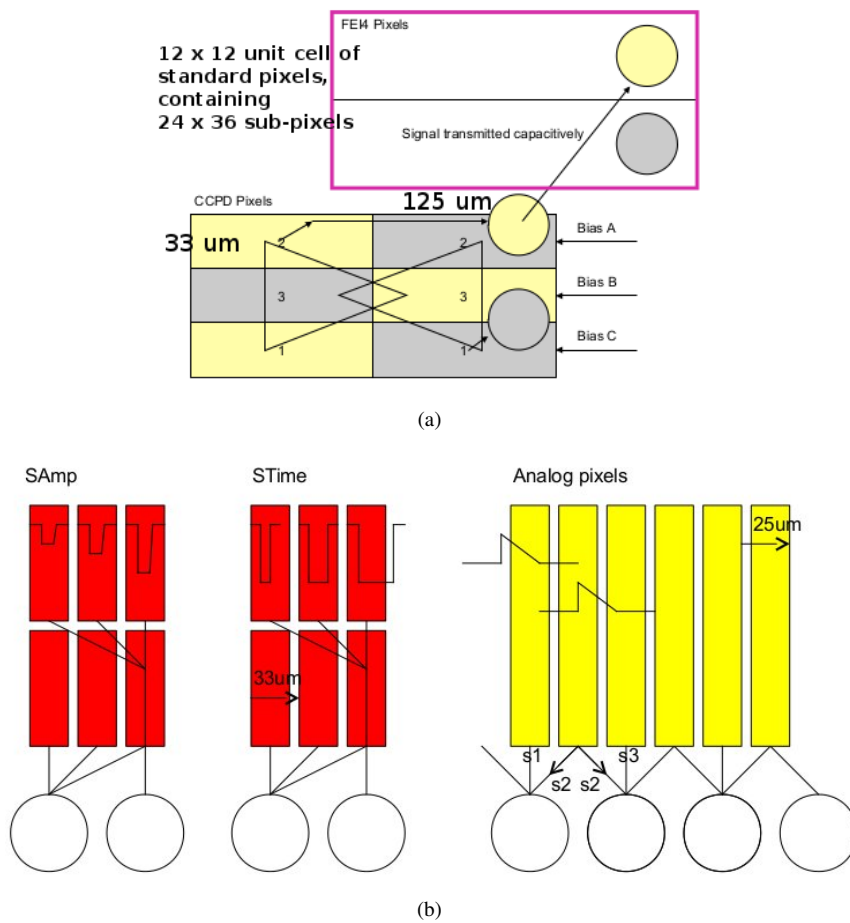


**Figure 3.7** – HV-CMOS pixels to FEI4 pixels (circle in the figure) connection. a) version 2. Three HV-CMOS pixels are connected to a FE-I4 pixel through a "chess pattern" to reduce charge sharing between connected pixels. b) version 4 for the different pixel flavors (STime and Analog pixels) [30].



A charged-tracker particle (telescope) has been designed and built by the University of Geneva in 2014. It has been successfully used in the CERN PS and SPS test-beam areas to measure the properties of several CCPD prototypes and it is currently being used at the SPS for the 2015 test-beam campaign.

### 4.1 The FE-I4 Telescope

An overall view of the telescope (referred hereafter simply as the FE-I4 telescope) is shown in figure 4.1. It is composed of two arms each hosting 3 planes instrumented with IBL double-chip planar modules, two scintillator planes for triggering and a movable stage (with a precision of the order of  $1\text{ }\mu\text{m}$  in X and Y axis, see figure 4.1) hosting the Device Under Test (DUT). Between the telescope arms, a DUT box of  $320 \times 170 \times 270\text{ mm}^3$  has been installed. The DUT box can be cooled thanks to an external chiller providing stable testing conditions.

In order to improve the resolution of the telescope in the long pixel direction (X), two planes have been rotated by  $90^\circ$  as shown in the picture. The Telescope resolution has been estimated using an analytic method [31] to be:  $\sigma_X=12\text{ }\mu\text{m}$  and  $\sigma_Y=8\text{ }\mu\text{m}$ .

With a single ATCA crate hosting the RCE system [32] and the optical link to the HSIO board [33] interfacing the planes, up to 8 FE-I4 chips can be read-out in parallel fitting perfectly the telescope application.

The trigger system can be centrally managed by the HSIO and the RCE module. Thanks to the FEI4 capabilities (see chapter 3), a signal can be directly sent to the trigger input when a telescope plane has registered an event, simplifying consequently the trigger hardware. During standard operation, signals from the first and last telescope planes are used in coincidence. The on-chip triggering, combined with a pixel mask matrix, allows to define a given Region Of Interest (ROI) at the triggering planes. This is especially suitable for small DUTs such as the CCPDs. The telescope trigger rate is  $\sim 10\text{ kHz}$  and it is fully synchronized with the DUT through the common DAQ.

### 4.2 The off-line reconstruction software

The reconstruction has been carried out using the JUDITH software framework [34]. Initially developed to analyze test-beam data of the Kartel telescope, it was subsequently adapted with success for the analysis of the FE-I4 telescope data.

The reconstruction is performed in different steps, namely: 1) clustering, 2) alignment of the telescope planes and DUT, 3) track reconstruction, 4) DUT data analysis.

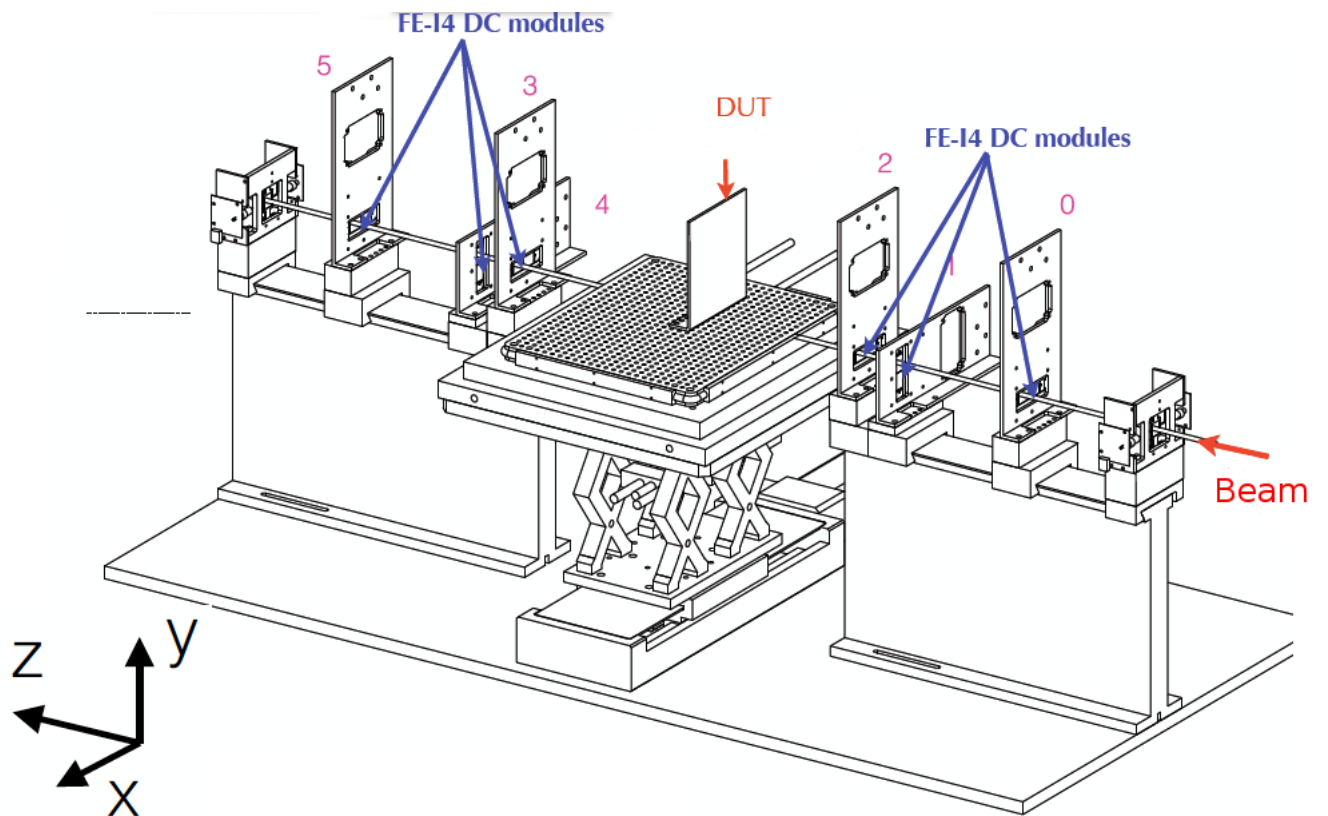
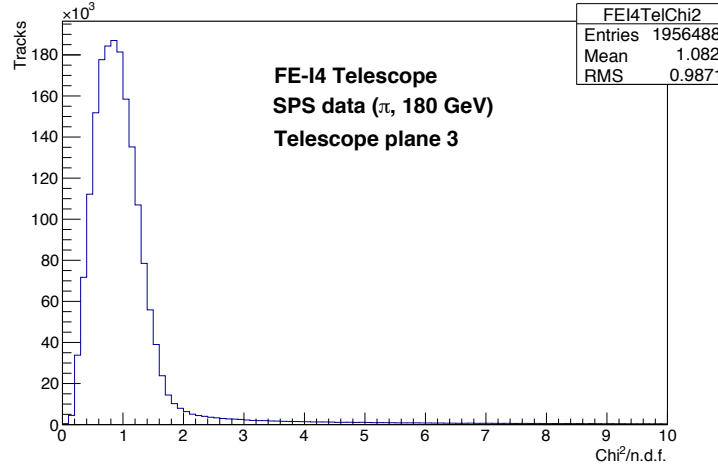


Figure 4.1 – FEI4-telescope layout [35].



Due to the charge sharing between pixels, a single particle hit can produce a cloud of fired pixels in a localised region of the detector. The clustering algorithm is an iterative procedure for adjacent pixels search. It groups several fired pixels into a single cluster. The position of the cluster is computed as its geometrical center (digital clustering, without taking into account charge information).

Once that clusters have been built in different planes, the traversing particle trajectory (track) can be reconstructed. The track reconstruction algorithm recursively searches for clusters on consecutive planes within a limited solid angle to avoid multiple scattering effects. The cluster positions on different planes are then fitted with a straight line. In our analysis, a cluster in all the 6 telescope planes associated to the track is requested. The  $\chi^2/n.d.f.$  distribution of reconstructed tracks is shown in figure 4.2. We select tracks with a  $\chi^2/n.d.f. < 3$ .



**Figure 4.2** –  $\chi^2/n.d.f.$  distribution of reconstructed tracks

The alignment of the telescope and DUT planes is done in two steps: 1) a coarse-alignment and 2) a fine-alignment. The first one corrects offsets in the two directions (X and Y, see figure 4.1) perpendicular to the beam. The first plane is kept fixed so that it represents a reference for the other planes. The cluster positions difference between the first and second plane is computed, the corresponding distribution is fitted with a gaussian and its mean is taken as offset of the second plane. Once that the offset of the second plane is fixed, the procedure is repeated for the third plane and subsequently it is repeated for all remaining planes.

The second step of the alignment procedure corrects small offsets and the rotation around the beam axis (z-axis). It is implemented using an iterative procedure based on unbiased<sup>1</sup> residuals; residuals are obtained by calculating the difference between the location where a track intercepts a sensor and the associated cluster in that sensor. The fine-alignment algorithm consists in two similar procedures, one for each measuring direction. Each plane is divided in slices along one direction (X for instance), residuals are computed along the other direction (Y) for each slice and fitted with a gaussian. The means of the gaussian distributions are then fitted with a straight line as shown in figure 4.3. The offsets and the rotation around the z-axis are computed, respectively, from the value of the fitted line at the center of the sensor (see figure 4.3) and from the fitted slope. Since the track parameters depend on the offsets and rotations that we are correcting for, this procedure is repeated iteratively. Figure 4.4 shows the reconstructed rotation along the beam axis, for a given telescope plane, as a function of the number of iterations up to its asymptotic value.

1. This means that the sensor for which the residuals are calculated is excluded from the track fit.

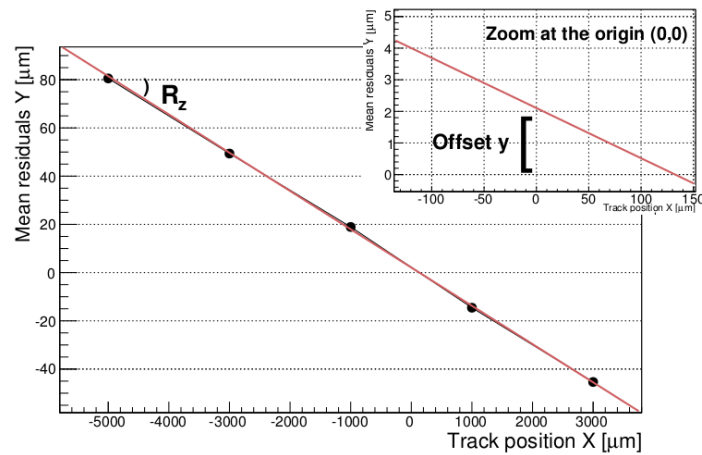
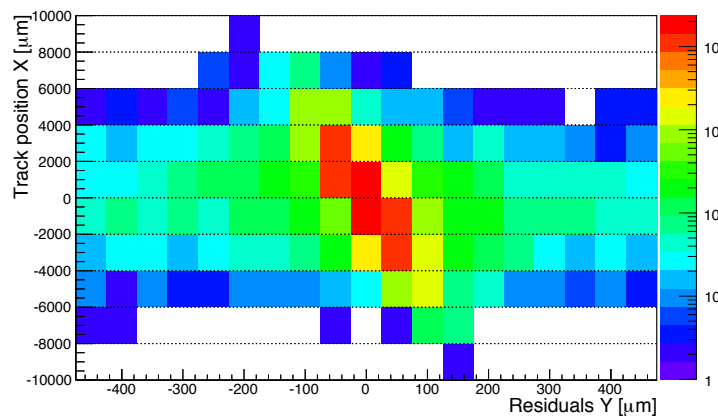
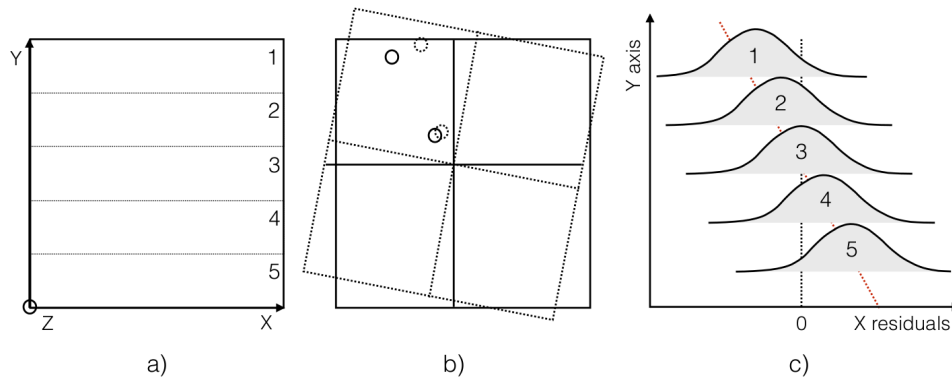


**Figure 4.3** – a) Schematic representation of the fine alignment procedure. On the left, the sensor is sliced in 5 sections along the y axis. In the centre, the predicted position of the sensor and the hits are represented as solid lines. Extrapolated hits and sensor position are shown in dashed lines. On the right, gaussian unbiased residuals distribution for each slice are represented as well as the linear fit to the gaussian means. b) Distribution of the residuals along Y vs track position along X. The plane is divided in slices (dashed lines) and for each of them residuals are computed and fitted with a gaussian. Because of a rotation of the plane ( $R_z$ ), the distribution shows a correlation between the two variables. c) Mean of the residuals for each slice as a function of the track position fitted with a straight line (red in the figure). Due to a small offset ( $\sim 2 \mu m$ ) the fitted line does not pass from the center of the sensor (0,0). This procedure is then repeated for the other direction (X).

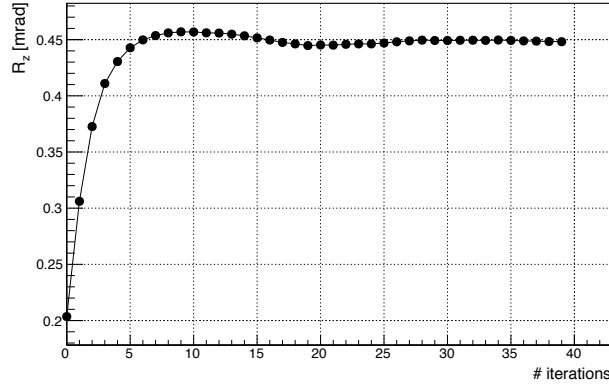


**Figure 4.4** – Rotation around the beam axis as extracted from the fine-alignment procedure for the third telescope plane as a function of the number of iterations.

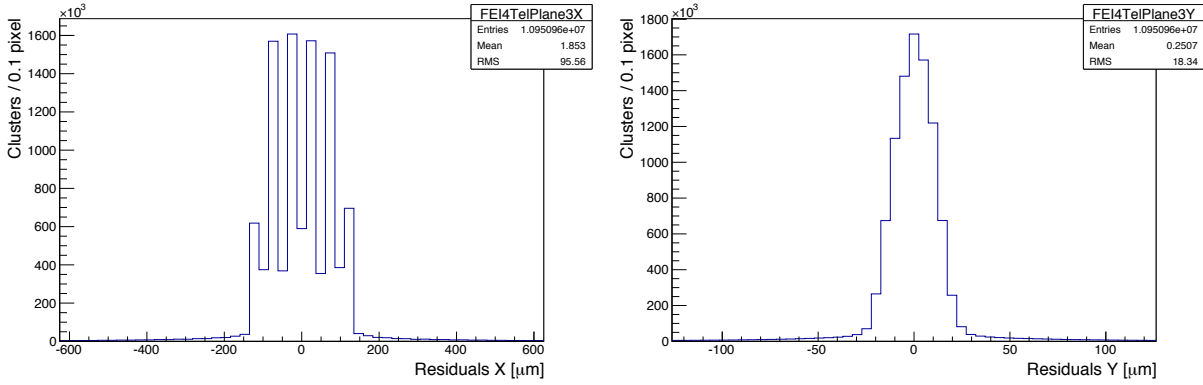


**Figure 4.5** – Residual distributions for plane 3 of the telescope.

Residual distributions are shown in figure 4.5 for plane 3 of the telescope. We note that they present a peaked structure along the long pixel direction (X). This feature has been studied in detail using simulations as discussed in the next chapter.

The final step of the algorithm is the DUT data analysis. In order to associate the DUT-cluster to a track, we extrapolate the fitted track to the DUT and compute:

$$d = \sqrt{\left(\frac{x_{track} - x_{DUT}}{l_X/2}\right)^2 + \left(\frac{y_{track} - y_{DUT}}{l_Y/2}\right)^2} \quad (4.1)$$

where  $l_{X(Y)}$  is the pitch of the sensor along the X (Y) direction,  $x_{track}$  and  $y_{track}$  are the extrapolated positions at the DUT,  $x_{DUT}$  and  $y_{DUT}$  are the DUT cluster positions. A minimum value for  $d$  is required to consider a track associated with the DUT cluster (matched tracks). In our analysis this minimum value is set at  $d=3$ .

The efficiency is then defined as:

$$\epsilon = \frac{N_{matched}}{N_{total}} \quad (4.2)$$

where  $N_{matched}$  is the number of matched tracks and  $N_{total}$  is the total number of reconstructed tracks.

### 4.3 Telescope simulation

Simulations have been run using a Geant4 [36] based software called AllPix [37].

The model used to simulate the FE-I4 Telescope is shown in figure 4.6. Each telescope plane is composed of an array of 80 rows, 336 columns, a pixel size of  $250 \times 50 \mu m^2$  and a thickness of  $200 \mu m$  to reproduce the FE-I4 planar pixel sensor matrix (see chapter 1), all the planes are perfectly aligned between each other. The simulated beam is made of  $180 \text{ GeV } \pi^+$  and no angular distribution has been simulated for the incoming particles.

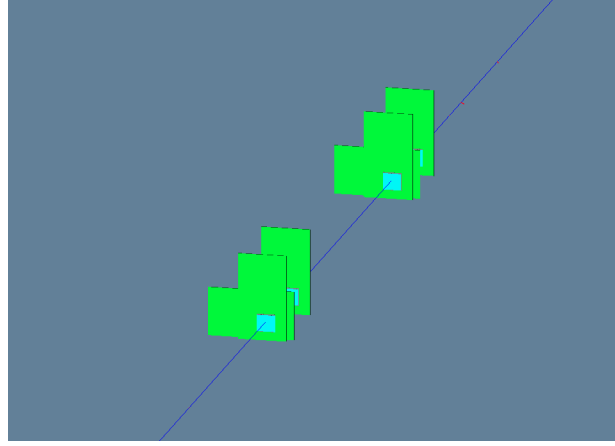


**Figure 4.6** – Overall layout of the simulated telescope. A  $180 \text{ GeV } \pi^+$  is visible in blue in the figure.

A pixel is considered as being fired if the energy released by the traversing particle is greater than a fixed threshold,  $E_{th} = 10 \text{ keV}$ . Simulated data have been converted into the JUDITH format and then analyzed in the same way as data. As shown in figure 4.7(a), residuals distribution presents 5 peaks equally spaced by  $50 \mu m$ . Due to the rectangular shape of the pixels ( $250 \times 50 \mu m^2$ ), the  $2 \text{ } 90^\circ$ -rotated planes give a granularity of 5 pixels with respect to the non-rotated ones giving pattern position to tracks. In the case of a perfectly aligned telescope the peaks are spaced by  $50 \mu m$ , but in the case of real data, offsets between planes might change the heights and the number of the peaks, as shown in figure 4.7.

A preliminary study aiming to understand the effect of the peaks in the resolution of the telescope is discussed in the appendix.

The simulation model developed for this thesis represents a starting point for future studies aiming to optimize the performance of the telescope.

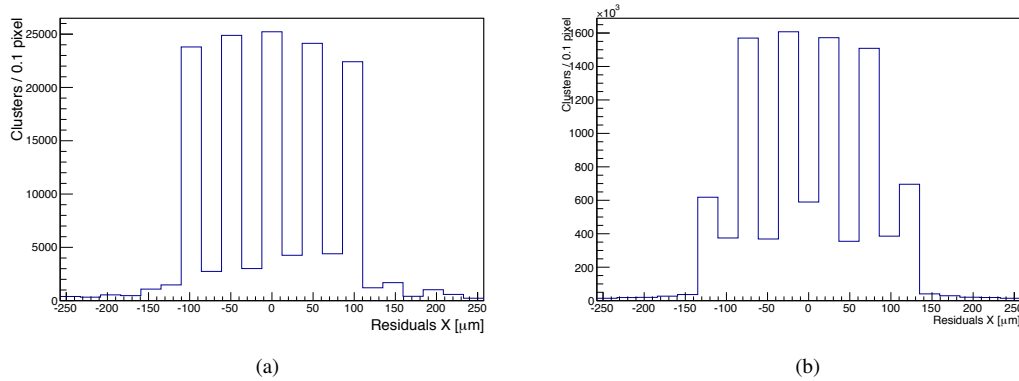


**Figure 4.7** – a) Residual distribution for plane 3 of the telescope from simulated data with a perfectly aligned telescope. b) Residual distribution for plane 3 of the telescope for real data. Due to offsets between planes, the distribution presents 6 peaks.

## 4.4 Results

More than 90 million triggers taken at the SPS between October and November 2014 have been analyzed. Different CCPD devices, irradiated and non-irradiated, have been studied (see table 4.1) in various configurations such as at different thresholds and bias voltages. It is worth reminding that the samples analyzed have different pixel flavors, as discussed in the previous chapter. In the following, I will show results of the *standard* pixels for the *v2* technology and the *Stime* pixels for the *v4* (unless otherwise specified), considering that they represent the most promising structures. The other pixel flavors were not tuned in these tests.

sample	irradiation	version	pixel type
C19	-	v2	standard pixels
C22	$10^{15} n_{eq}/cm^2$	v2	standard pixels
402	-	v4	stime & analog
404	$10^{15} n_{eq}/cm^2$	v4	stime & analog

**Table 4.1** – CCPD prototypes measured at the SPS test-beam and their characteristics.

At the time the test-beams were being performed, the HV-CMOS pixels decoding (see chapter 3, figure 3.7) was not implemented into the readout. Therefore, each pair of FE-I4 pixels have been merged, along the Y direction, resulting in a virtual pixel of  $250 \times 100 \mu m^2$  size containing 6 HV-CMOS pixels.

Due to a systematic early breakdown, the bias voltage could not be increased more than 12 V and 35 V for the non-irradiated CCPDv4 (402) sample and for the irradiated one (404) respectively. The non-irradiated CCPDv2 (C19) and the irradiated (C22) have been tested at a bias voltage of 90 V and 80 V.

Residual distributions for all the analyzed samples are shown in figure 4.8.

In the following I will discuss the efficiency and timing studies for the four analyzed samples.

### Efficiency studies

The efficiency map of the four samples is shown in figures 4.9 and 4.10. The non-irradiated CCPDv2 (C19) presents one less efficient pixel. This is due to the fact that during data taking, two out of the six HV-CMOS pixel have been disabled resulting in an efficiency of  $\sim 66\%$  in that single pixel. The irradiated *v2* sample (C22) shows two pixels with an efficiency of  $\sim 50\%$ ; for each of them, one of the two FE-I4 pixels was disabled during data taking, owing to the irradiation effects to the corresponding HV-CMOS pixels. The irradiated *v4* (404) presents two pixels rows that have not been tuned during data taking.

The efficiency of a device is calculated as the average of the single pixel efficiencies. Table 4.2 summarized the efficiency for the samples taken into analysis.

sample	efficiency	bias voltage	threshold
C19	$(99.6 \pm 0.2)\%$	90 V	0.94 V
C22	$(95.4 \pm 0.4)\%$	80 V	0.93 V
402	$(99.5 \pm 0.2)\%$	12 V	0.84 V
404	$(96.5 \pm 0.3)\%$	30 V	0.83 V

**Table 4.2** – Efficiency, bias voltage and threshold for the four analyzed prototypes.

Bias scan and Threshold scan have been performed for the CCPDv4 samples as shown in figure 4.11. The non-irradiated sample (404) presents a very high efficiency even at 0 V ( $\epsilon = 99.1\%$ ), suggesting the presence of a diffusion component in the charge collection mechanism. For the irradiated sample, instead, the diffusion is strongly reduced due to the high trap density (see chapter 2) which enhances the capture of the diffusing slow carriers. Therefore, for the irradiated sample, charge collection occurs mainly by drift, resulting in a drop of efficiency for low values of the bias voltage. As expected, the efficiency increases with the bias voltage (as due to the increase of both the width of the depletion region and the electric field in the bulk). Since the plateau

of the curve is not reached, improvements of the performance of the detector are expected for higher values of the bias voltage.

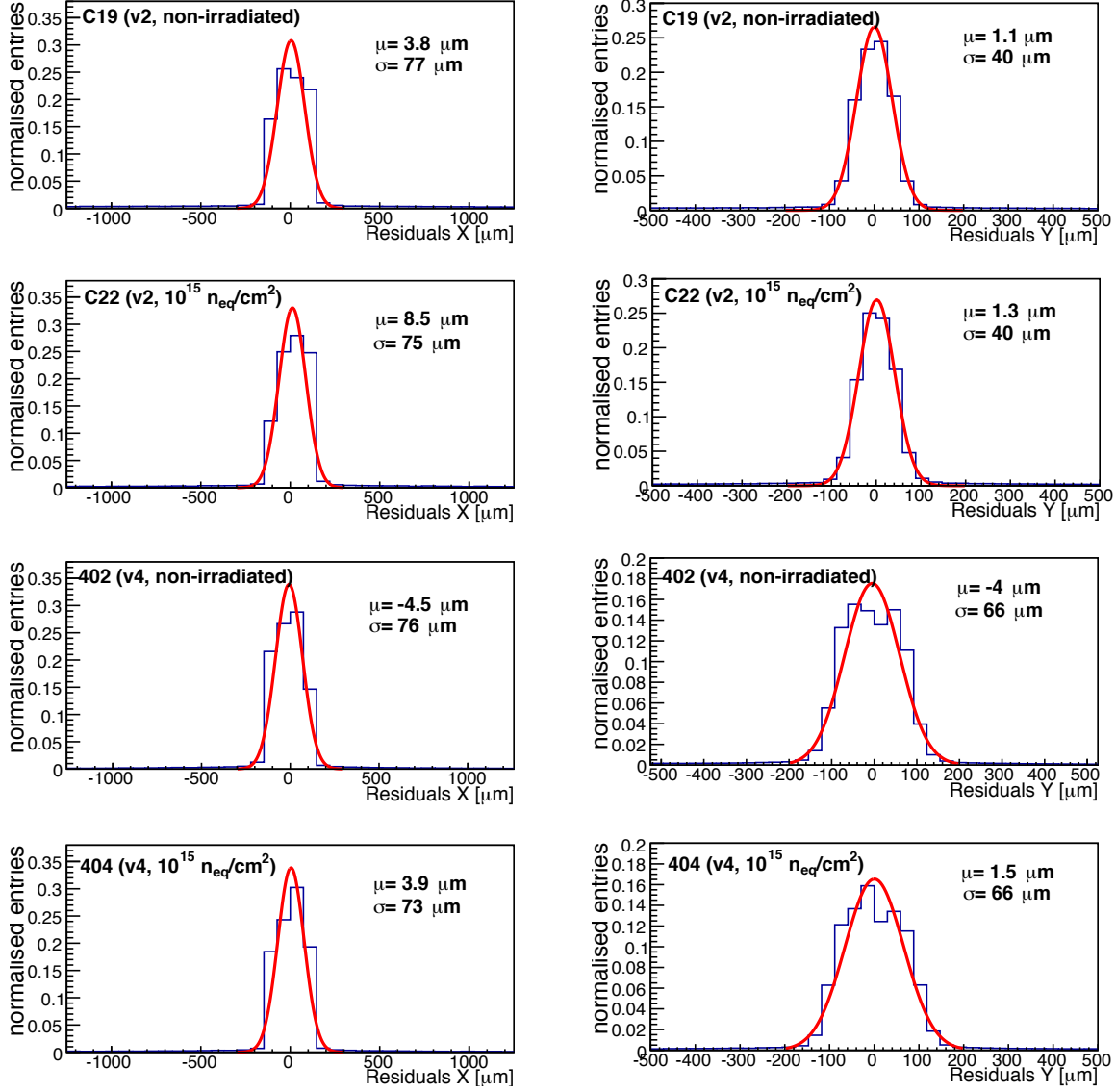
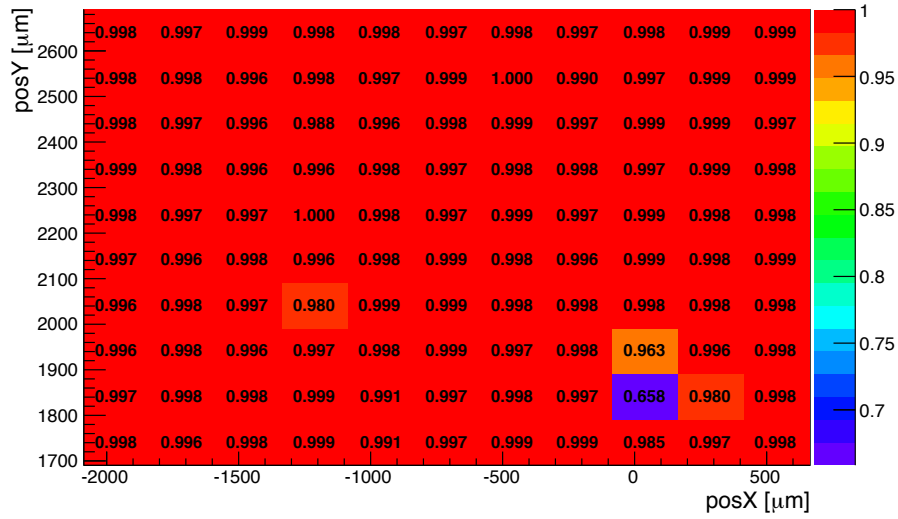
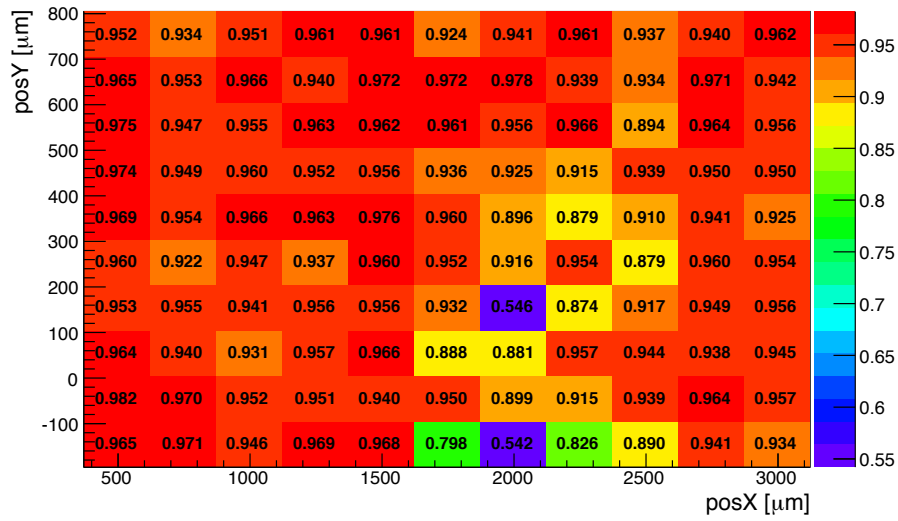


**Figure 4.8** – Residual distributions for the four samples analyzed. Due to the small size of the DUTs and the large pixel size ( $100 \times 250 \mu\text{m}^2$ ), the alignment procedure did not correct small offsets and rotation. In particular, owing to the smaller size of the *Stime* pixel arrays (402 and 404 prototypes) we observe that the residual distributions are broader, in the short pixel direction (Y), compared with the distributions of the other prototypes (C19 and C22 prototypes).

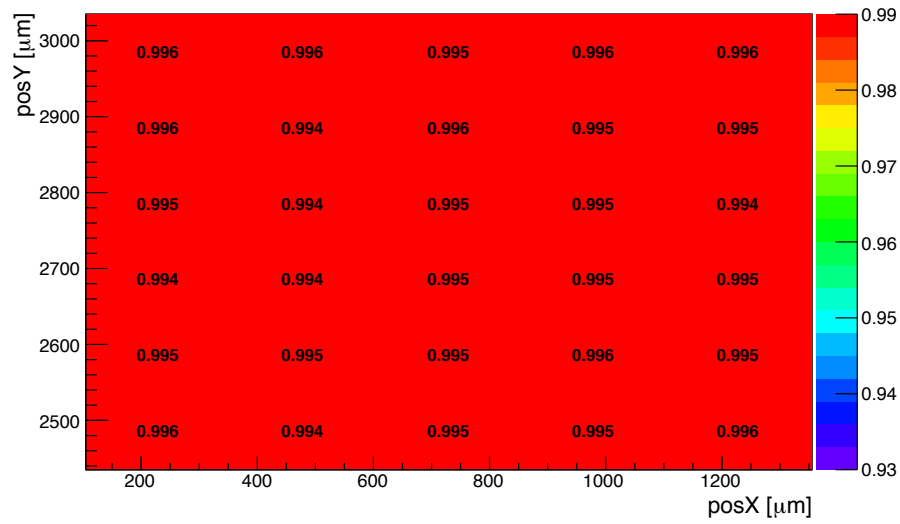


(a) C19 Efficiency map.  $HV_{bias}=90$  V,  $Th.=0.94$  V

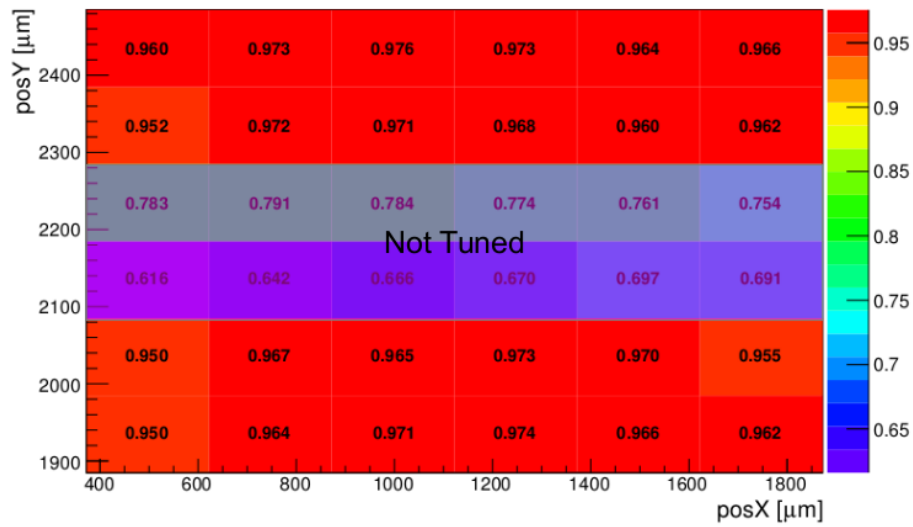


(b) C22 Efficiency map.  $HV_{bias}=80$  V,  $Th.=0.93$  V

**Figure 4.9** – Efficiency maps for the  $v2$  samples C19 (a) and C22 (b). C19 presents one pixel with an efficiency of  $\sim 66\%$ , during data-taking two out of the six HV-CMOS pixel have been disabled for that single pixel. C22 shows two non-working pixels due to the irradiation effects, these pixels and their neighbors have been excluded in the calculation of the efficiency of this device.



(a) 402 Efficiency map.  $HV_{bias} = 12$  V,  $Th. = 0.84$  V



(b) 404 Efficiency map.  $HV_{bias} = 30$  V,  $Th. = 0.83$  V

**Figure 4.10** – Efficiency map for the  $v4$  samples 402 (a) and 404 (b). As shown in the figure, for the 404 sample two rows were not tuned during this test and therefore not taken into account for the computation of the efficiency of this sample.



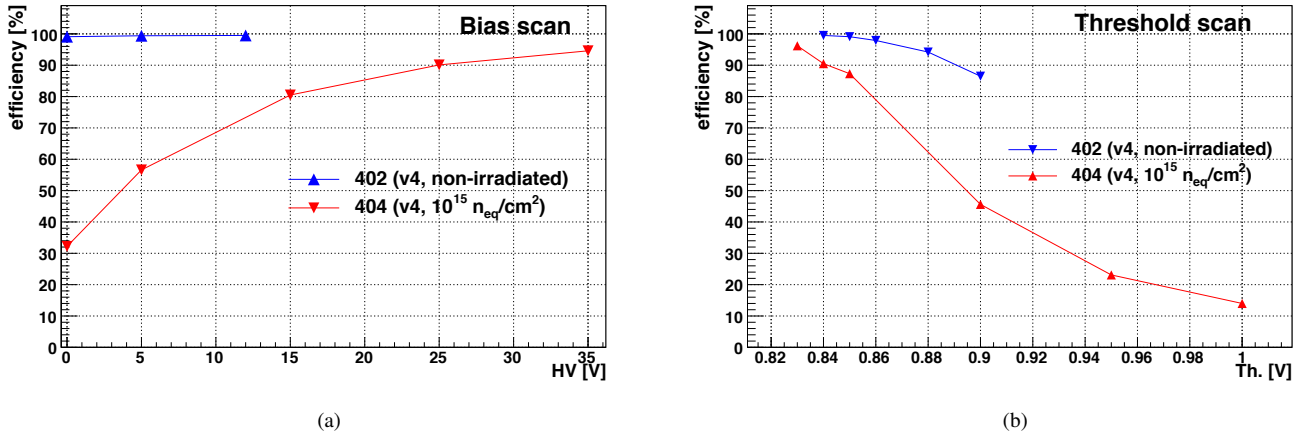


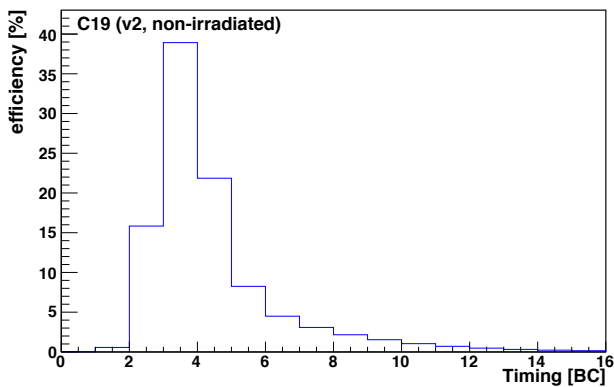
**Figure 4.11** – a) Bias scan (Threshold= 0.84 V for both prototypes). b) Threshold scan (HV= 12 V for the 402 prototype and HV= 30 V for the 404 prototype ).

### Timing studies

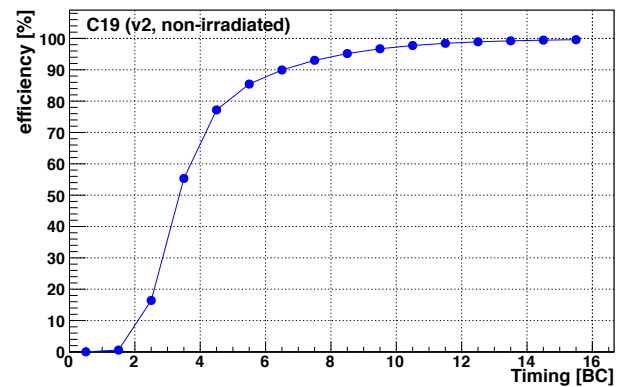
The efficiency as a function of the time response<sup>2</sup> of the detector has been studied for the samples in analysis. As shown in figure 4.12 and 4.13, the distribution of the non-irradiated CCPDv2 (402) and CCPDv4 (404) show long tails. An efficiency of around 99 % is reached in  $\sim 15$  b.c. On the contrary, figures 4.14 and 4.15 show that for the irradiated *v2* sample (C22) and for the irradiated *v4* sample (404), the efficiency no longer increases for high timing values ( $\sim 7$  b.c.). This fact could be explained by the slow diffusion component which affects the efficiency of the non irradiated sensor, as previously mentioned.

For the irradiated sample (see figure 4.15), the efficiency increase significantly with the applied voltage, reaching an efficiency of 88 % in the first 4 b.c. (for a bias voltage of 35 V). On the other hand, simulations (see the next chapter) show that the time needed to collect drifting carriers is of the order of 20 ns. This fact gives us confidence that the on-chip electronics of the HV-CMOS samples might influence the collection time of the CCPDs. In order to study this effect, we analyzed the timing distribution for different thresholds. As shown in figure 4.16, the peaks of the distributions are shifted for different thresholds, suggesting the presence of a time-walk effect. This effect have been demonstrated studying the analog pixels. Figure 4.17 shows the 2D distribution of the timing vs the ToT for the irradiated *v4* prototype (404), the time walk is evident as there is an anti-correlation between the two quantities. As the analog pixels do not have a comparator in their in-pixel electronics, the origin of the time-walk effect is in the in-pixel pre-amplifier. The change of the rise and fall time at the output of the pre-amplifier for different heights of the incoming signal produces this effect, at the comparator level, when a threshold is applied.

<sup>2</sup>. The timing response of the DUT is defined as the difference between the initial trigger time of the telescope and the time when a hit in the DUT is recorded.

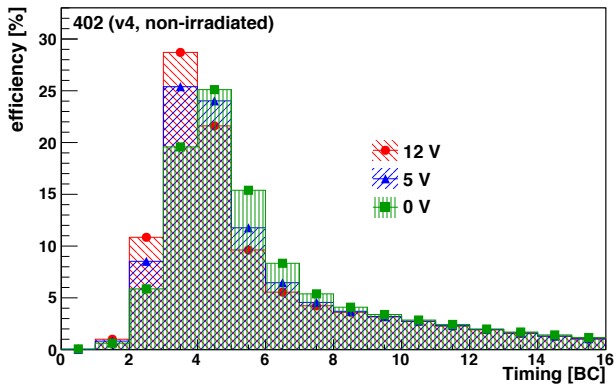


(a)

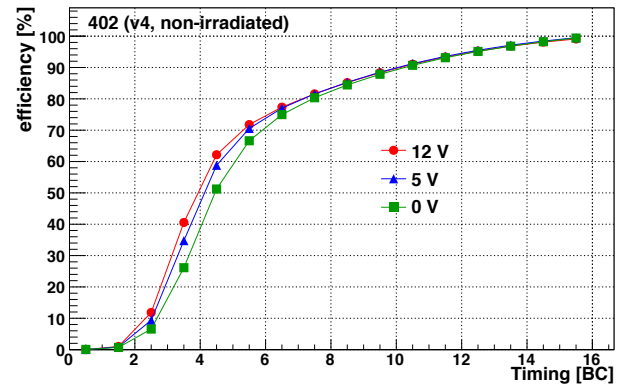


(b)

**Figure 4.12** – a) Efficiency as a function of the timing for the C19 sample biased at 90 V ( $\text{Th.} = 0.94$  V). Each Bunch Crossing (BC) unit-bin corresponds to 25 ns. b) cumulative efficiency for the same sample.

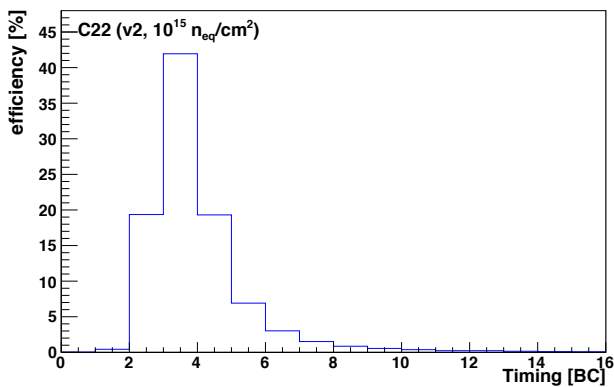


(a)

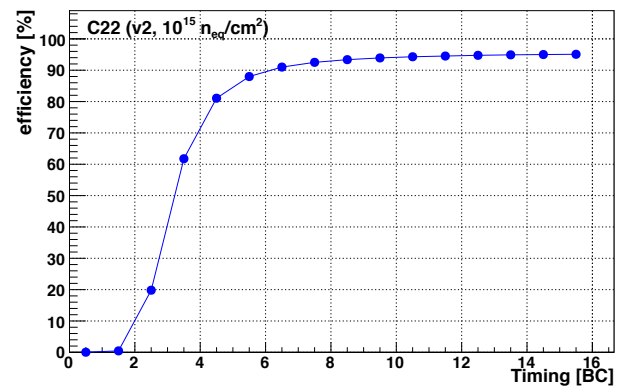


(b)

**Figure 4.13** – a) Efficiency as a function of the timing for the 402 sample for different values of the bias voltage ( $\text{Th.} = 0.84$  V). Each BC unit-bin corresponds to 25 ns. b) cumulative efficiency for the same sample.



(a)



(b)

**Figure 4.14** – a) Efficiency as a function of the timing for the C22 sample biased at 80 V ( $\text{Th.} = 0.93$  V). Each Bunch Crossing (BC) unit-bin corresponds to 25 ns. b) cumulative efficiency for the same sample.

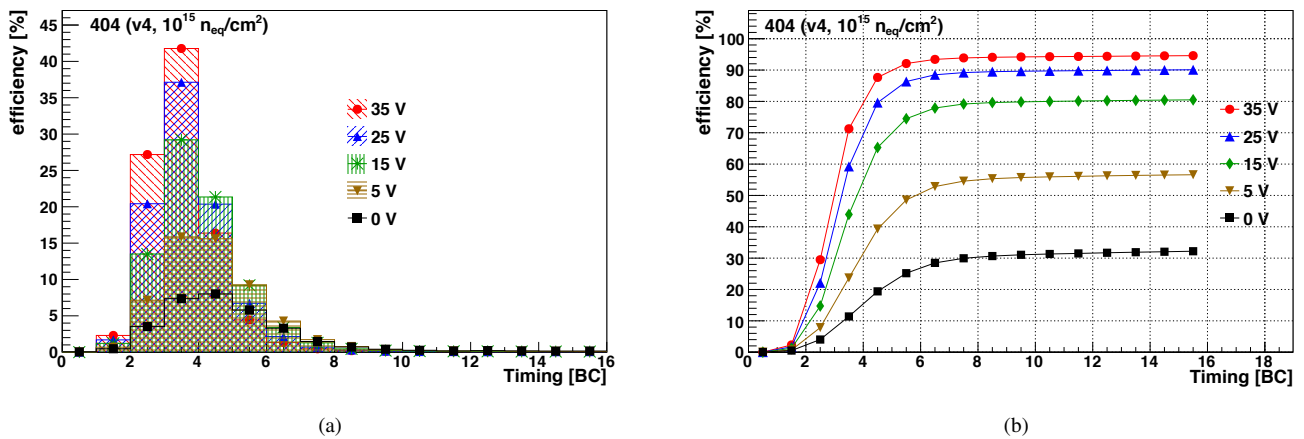


**Figure 4.15** – a) Efficiency as a function of the timing for the 404 sample for different values of the bias voltage (Th.= 0.84 V). Each BC unit-bin corresponds to 25 ns. b) cumulative efficiency for the same sample.

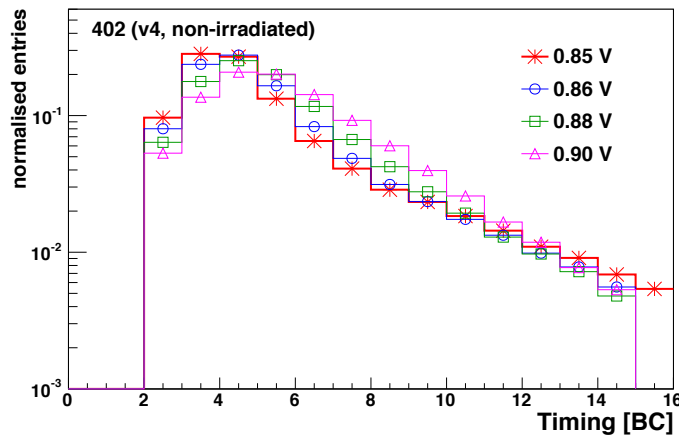


**Figure 4.16** – Normalised distribution of the timing for the 402 sample biased at 12 V for different threshold values. The peaks of the distributions are shifted for different threshold suggesting a time-walk effect.

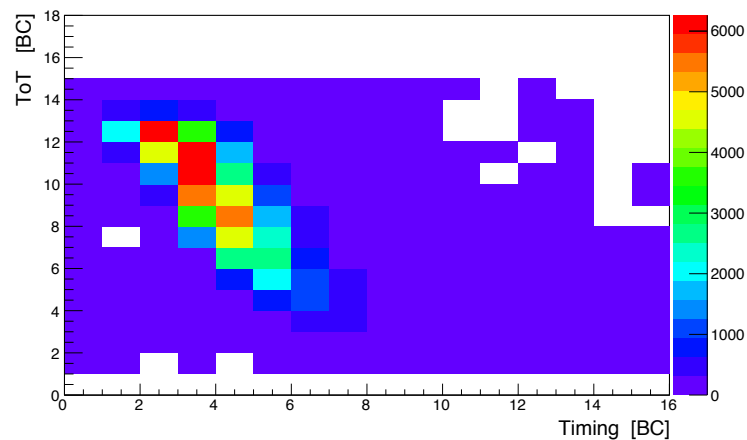


**Figure 4.17** – ToT vs Timing distribution of the 404 prototype (biased at HV= 35 V, Th.= 0.84 V) for the analog pixels (no comparator is present in the on-chip electronics, see chapter 3).

## Summary

Four CCPD prototypes, irradiated and non-irradiated, have been analyzed. The non-irradiated CCPDv2 (C19) and CCPDv4 (402), and the irradiated CCPDv4 (404) show a good efficiency: 99.6 %, 99.5 % and 96.5 % respectively. The irradiated *v2* sample (C22) presents some non-working pixels due to the irradiation effects. These pixels and their neighbours have been excluded from the computation of the efficiency of the device, resulting in an efficiency of 95.4 %. Bias and threshold scan have been performed for the *v4* prototypes. Comparing the results of the irradiated and non-irradiated prototypes we observed the presence of a diffusion component in the charge collection mechanism of the non-irradiated DUTs. Due to irradiation effects, such a component is strongly reduced for the irradiated CCPDs. Because of this fact, the efficiency of the irradiated sample drops at low values of the bias voltage.

The timing studies have shown long tails in the distributions of the two non-irradiated prototypes (C19 and 402). An efficiency of around 99 % is reached in  $\sim 15$  b.c. In the case of the irradiated sample, instead, the overall efficiency is reached in  $\sim 8$  b.c. ( $\epsilon = 95.4$  % for the C22 prototype biased at HV= 90 V and  $\epsilon = 94.6$  % for the 404 prototype biased at HV= 35 V). We addressed this fact to the slow diffusion component which is mostly affecting the non-irradiated samples and to a time-walk effect, generated at the on-chip pre-amplifier which enlarges the time response for both irradiated and non irradiated prototypes.

It is worth reminding that the *v4* prototypes 402 and 404 have been tested, due to a systematic early breakdown, at a maximum bias voltage of 12 V and 35 V respectively. Improvements in terms of efficiency and timing are expected for higher values of the bias voltage.

ITk requirements demand an overall efficiency of  $\sim 99$  % in the first 2 b.c. Even if this is not found in the analyzed samples, results show that improvements in the performance of the DUTs are possible. The upcoming prototype is expected to address the issues revealed by this study.

Technology Computer-Assisted Design (TCAD) is a finite element simulator which allows to find an approximate solution of a system of coupled partial differential equations. Finite element simulation is based on a variational form of the differential equations that allows to describe the problem in terms of a linear system of equations that can be solved by linear algebra methods. The approximation is then carried out subdividing the surface or volume in rectangular, triangular, prismatic or pyramidal sub-elements, small enough that the solution is locally polynomial in this domain. The interested reader can find a more detailed description of finite element simulations elsewhere [38].

This tool can be used to simulate semiconductor devices and in particular, it can be used to simulate the fabrication process of a silicon device as well as its electrical properties. I joined a collaboration between the U. of Geneva, U. of Liverpool, CERN and LAL<sup>1</sup> aiming to optimize the design of the upcoming HV-CMOS AMS 350 nm full-demonstrator chip, foreseen for September 2015.

In the following I will describe the sensor layout and the physical models used in simulations, I will then present and discuss the results.

### 5.1 The model layout

Several prototypes are expected to be realized with different substrate resistivity: 20  $\Omega\text{cm}$ , 80  $\Omega\text{cm}$ , 200  $\Omega\text{cm}$  and 1000  $\Omega\text{cm}$ . For all of them the basic pixel structure is the same and it is shown in figure 5.1.

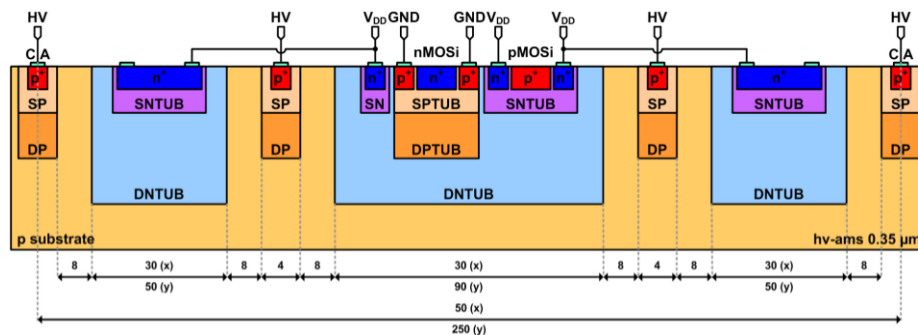


**Figure 5.1** – Model layout of a single pixel of the HVCMOS AMS prototype [39]. Units are in  $\mu\text{m}$ . The three sub-pixels are connected to a common read-out. The deep n-well (DNTUB) hosts a shallow n-layer (SNTUB) and a shallow p-layer (PNTUB). The bias electrodes are located on the top of the of the shallow p-layer situated among sub-pixels (SP and SP).

1. Laboratoire de l'Accélérateur Linéaire (Orsay, France).

The pixel is designed to be  $250 \times 50 \mu m$  to match an FE-I4 pixel (see chapter 3). It is divided into 3 sub-pixel in order to reduce the input capacitance [39]. The central deep n-well (DNTUB) hosts a shallow n-well (SNTUB) and p-well formed of two layers with different doping concentration (DPTUB and SPTUB). Transistors are located within these shallow doped regions. The three sub-pixels are connected to a common read-out. The bias electrodes are located at the top of the shallow p-layers (DP and SP) in between two sub-pixels.

Since we do not have access to the details of the fabrication process procedure and its parameter (e.g. annealing time and temperature), a process simulation might add complexity and led to wrong doping profile. Therefore, the simulated layout has been carried out using analytic functions. The overall simulated layout is shown in figure 5.2 and the simulated doping profile in figure 5.3.

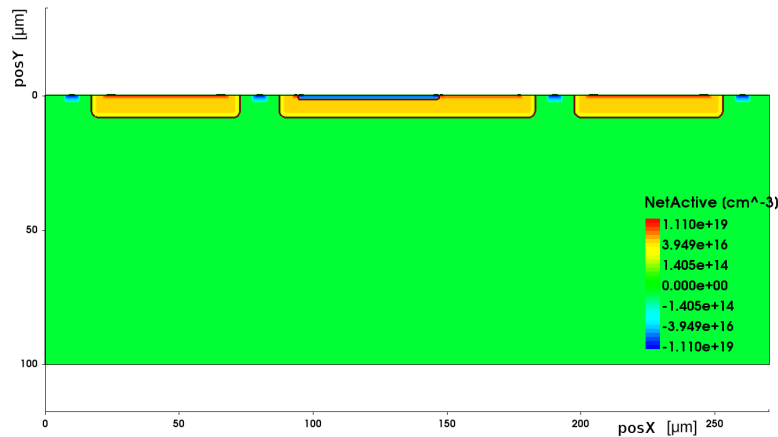
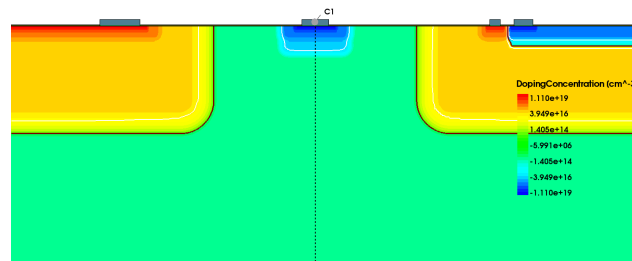
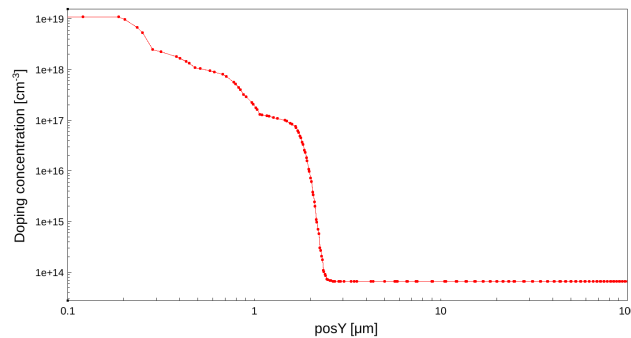


**Figure 5.2** – Overall view of the simulated pixel structure (see figure 5.1) . A  $\sim 2 \mu m$   $SiO_2$  layer has been implemented at the top of the device. Transistors have not been simulated.



(a)



(b)

**Figure 5.3** – a) Detail of a bias electrode. The shallow doping profile are shown. b) Doping profile along the center of the p-layer.

## 5.2 Physics model

TCAD simulations used in semiconductor devices solve numerically the Poisson equation and the continuity equation for electrons and holes:

$$\begin{cases} \frac{dp}{dt} - \nabla \cdot \vec{J}_p = G_h - R_h \\ \frac{dn}{dt} - \nabla \cdot \vec{J}_n = G_e - R_e \\ -\Delta V = \frac{\rho}{\epsilon} \end{cases} \quad (5.1)$$

with

$$\vec{J}_n = -\mu_n n \nabla V + D_n \nabla n \quad ; \quad \vec{J}_p = -\mu_p p \nabla V + D_p \nabla p \quad (5.2)$$

where  $n$  ( $p$ ) is the electron (hole) density,  $\mu_{n(p)}$  is the electron (hole) mobility,  $D_{n(p)}$  is the diffusivity constant for electron (hole),  $\vec{J}_{n(p)}$  is the current density,  $G_{e(p)}$  is the electron (hole) generation rate and  $R_{e(p)}$  the recombination rate.

Three types of boundary conditions have been implemented in our model. In the semiconductor/insulator boundary the current is not allowed to flow through this surface and therefore the Von-Neumann boundary condition is applied. On the contrary, the metal-semiconductor surfaces are the boundaries between the silicon bulk and the metallic electrodes, this is usually a ohmic contact and the current is allowed to flow through them. The voltage  $V$  is constant and equals the bias voltage applied to the sensor by an external power supply and for these reason, a Dirichelt boundary condition has been applied.

Guard ring structures are metal semiconductor interfaces where the metallic electrode is self-biased. To represent this case, we must impose a null current flow on this contact. The bias voltages taken by the floating contacts are then found by the solver of the TCAD software.

We now need to characterize the variable in equation 6.1 (mobility, generation and recombination rates). To do so, TCAD software offers a large variety of different models. In most of the cases these models are phenomenological parametrization of experimental data for different conditions of the device in analysis (e.g. doping concentration, temperature of operation, dimension of the device). We used the following models in our simulation:

- **Mobility** Masetti model [40]: degradation of the mobility due to scattering through the impurities.
- **Mobility** Canali model [41]: velocity saturation due to high electric field.
- **Recombination** SRH model [24]: generation/recombination occurs through shallow traps in the band due to the impurities. The carriers lifetime has been increased to  $\tau = 10^{-6} \mu s$  because of the high purity of the silicon expected for the new prototype.
- **Recombination** Scharfetter relation [42] : recombination lifetime degradation due to impurities.
- **Band gap narrowing** SlotBoom model[43]: decrease the gap for highly doped substrate.

Furthermore the energy released from the incoming particle is modelled using a Linear Energy Transfer (LET) function as shown in figure 5.4. The LET function is expressed by the following relation:

$$G(l, w) = G_{LET}(l) R(w, l) \quad (5.3)$$

where  $l$  is the longitudinal direction w.r.t. the incoming particle,  $w$  is the transverse direction,  $G_{LET}(l)$  is the linear energy transfer generation density,  $R(w, l) = \exp(-\frac{w}{\sigma_w})$  is the spatial distribution in the transverse direction. Table 5.1 shows the value used in simulation.

Due to the approximation of the LET function within mesh elements, the value of  $G_{LET}(l)$  might change significantly leading to a difference of the generation density w.r.t. the initial value given in simulation. We

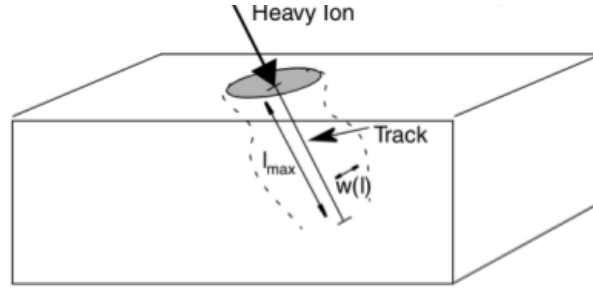


**Figure 5.4** – A particle penetrating a semiconductor; its track is defined by a length and the transverse spatial influence is assumed to be symmetric about the track axis [23].

Paramter	Units	Value
$G_{LET}(l)$	$e^-/h$ pairs per $\mu$ m	80
$\sigma_w$	$\mu$ m	0.05

**Table 5.1** – LET parameters [23].

implemented different meshing strategies<sup>2</sup> and we verified that this fact does not influence the overall interpretation of the results. It compromises, however, a quantitative estimation of the results. The simulated data should be tuned with experimental data to have access to this information. Therefore the results presented in the next section must be interpreted as a qualitative estimation of how the performance of the detector varies for different design parameters.

### 5.3 Results

Simulations have been performed for different biasing voltages and resistivities (20, 80, 200, 1000  $\Omega$ cm). The depletion depth is shown in figure 5.5. The depth increases linearly with the square root of the bias voltage as expected:  $d \propto \sqrt{\rho V}$  (see chapter 2). The distribution of the electric field is shown for different resistivities in figure 5.6. We note that for low resistivities, 20  $\Omega$ cm and 80  $\Omega$ cm, the distribution is homogeneous within the depletion zone. For 200  $\Omega$ cm and 1000  $\Omega$ cm, instead, the absolute value of the electric field is large enough to produce a high depletion depth, but its strength is mostly concentrated among the p-implant and the deep n-well resulting in a low field in the vicinity of the depletion region (white line in the figures). Figure 5.7 shows the field line of the device in analysis. Since the line integral must give the bias voltage:  $\int_l E(x, y) dl = \Delta V_{bias}$ , it is clear that in the region between the bias electrode and the collecting electrode, where the field lines have the shortest path, the electric field is large. On the contrary, in the case of the deep-bulk region the field lines must come back to the collecting electrode, such that:  $l_{field} \propto 2d_{depletion}$  resulting in a low-field region. We note that in the case of 20  $\Omega$ cm and 80  $\Omega$ cm the depletion is small and this effect is reduced.

In order to study how this feature influences the charge collection mechanism, a *mip* passing through the center of the pixel has been simulated. Figure 5.8 shows the induced current at the collecting electrode for different resistivities. At the initial time of the interaction<sup>3</sup>, the collected charge is larger for 20  $\Omega$ cm and 80  $\Omega$ cm compared to the higher resistivity values: 200  $\Omega$ cm and 1000  $\Omega$ cm. For these resistivities the electric field is low in the deep-bulk region and the charge collection mechanism is slow. This effect is particularly evident for 1000  $\Omega$ cm. Figure 5.9 shows the evolution of the electrons distribution for different time intervals for a simulated device of 1000  $\Omega$ cm biased at 50 V. We note that the electric field is not sufficient to fully collect the charge and therefore the collected signal slowly increases with the time because of the diffusing slow carriers.

2. A finer mesh around the particle track has been implemented. This refinement has been implemented using the *RecBoxInteger* meshing model. The interested reader can find more details here [23].

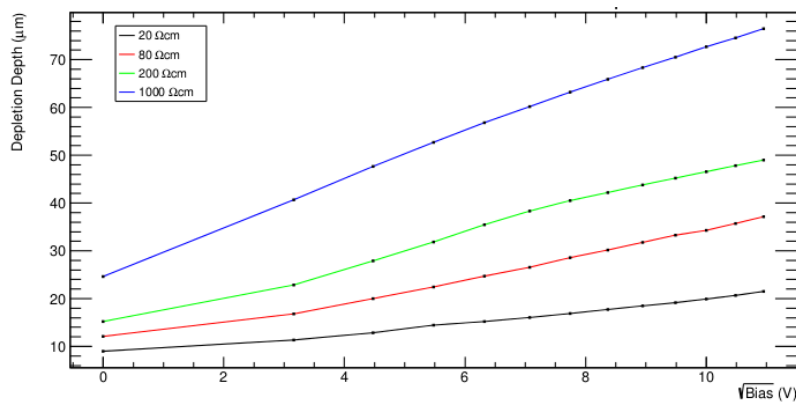
3. The time that a *mip* needs to pass through the simulated structure is of the order of fs. Since we are interested in effect which in takes place in  $\sim$  ns, the interaction is considered instantaneous.



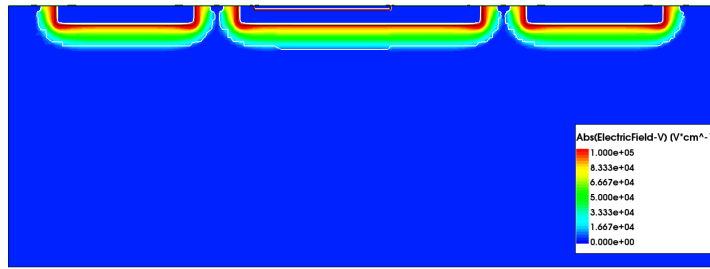
In order to investigate the differences between the top bias and a back bias solution, we implemented a back-bias electrode, leaving the previous electrodes at the top of the structure as floating contacts. Furthermore, we have added a p-doped layer with a thickness of  $2\ \mu\text{m}$  at the back of the device to avoid a direct metal-semiconductor contact (Schottky diode).

Figure 5.10(a) shows the field line for a back biased device with a resistivity of  $1000\ \Omega\text{cm}$  biased at  $50\ \text{V}$ ; as expected the lines assume a vertical shape running from the collecting to the bias electrode. Figures 5.10(b) and 5.10(c) show the induced current at the collecting electrode for different time intervals. In accordance with what is mentioned above, the effect analysed in the case of top biasing is removed and the device behaves as a standard planar detector, where, the collected charge increases with the depletion depth and thus with the resistivity.

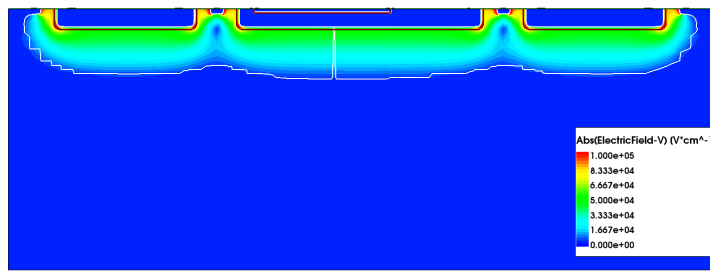
In conclusion, when top bias is applied, the low resistivity substrates ( $20\ \Omega\text{cm}$  and  $80\ \Omega\text{cm}$ ) present a faster collection time and a larger collected signal (in a time interval of  $\sim 60\ \text{ns}$ ) compared to the higher resistivity substrates ( $200\ \Omega\text{cm}$  and  $1000\ \Omega\text{cm}$ ). On the contrary, in the case of back bias, we observe that for higher resistivity values we have larger collected signal and, in particular, for a simulated device with a resistivity of  $1000\ \Omega\text{cm}$ , biased at  $50\ \text{V}$ , the charge is fully collected in  $\sim 10\ \text{ns}$ .



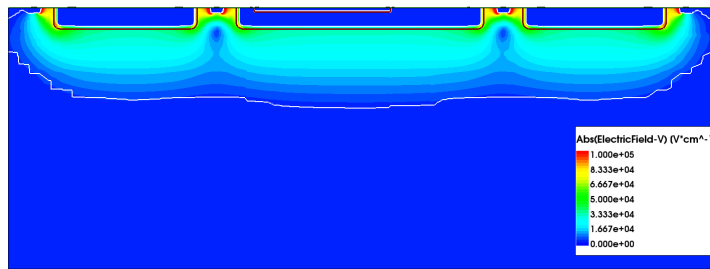
**Figure 5.5** – Depletion depth computed at the center of the pixel for different bias voltages and resistivities.



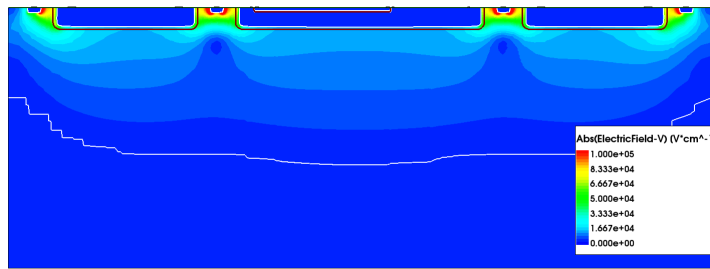
(a)  $\rho = 20 \, \Omega\text{cm}$  and  $HV_{bias} = -50 \, \text{V}$ .



(b)  $\rho = 80 \, \Omega\text{cm}$  and  $HV_{bias} = -50 \, \text{V}$ .



(c)  $\rho = 200 \, \Omega\text{cm}$  and  $HV_{bias} = -50 \, \text{V}$ .



(d)  $\rho = 1000 \, \Omega\text{cm}$  and  $HV_{bias} = -50 \, \text{V}$ .

**Figure 5.6** – a) Distribution of the absolute value of electric field within the pixel structure for different resistivities.

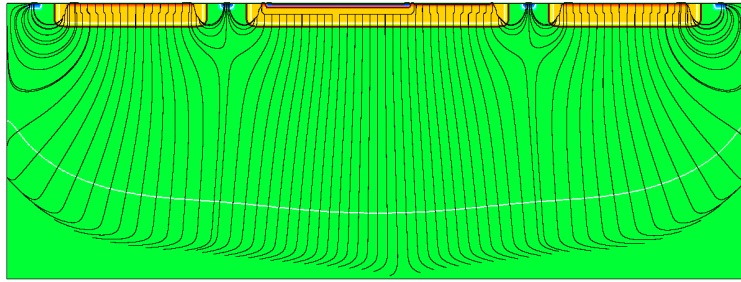
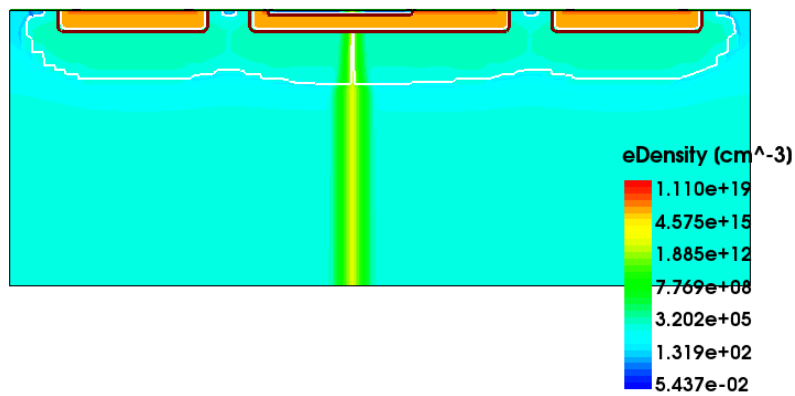
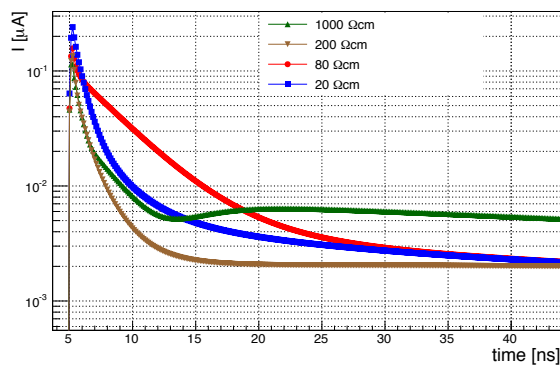


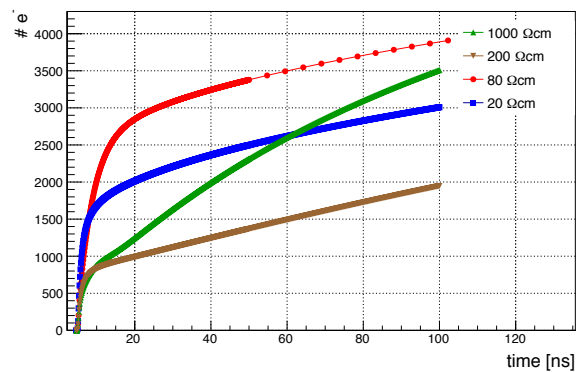
**Figure 5.7** – Field lines for a simulated device with a resistivity of  $\rho = 1000 \, \Omega\text{cm}$  biased from the top of the device with  $HV_{bias} = -120 \, \text{V}$ .



(a)



(b)

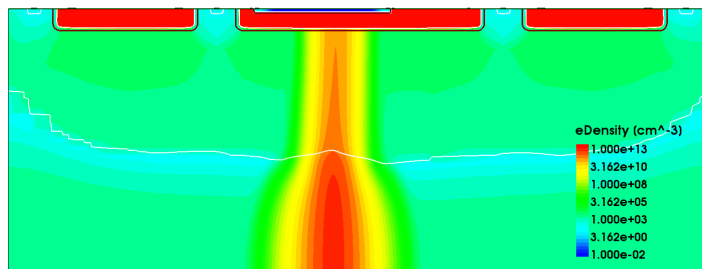


(c)

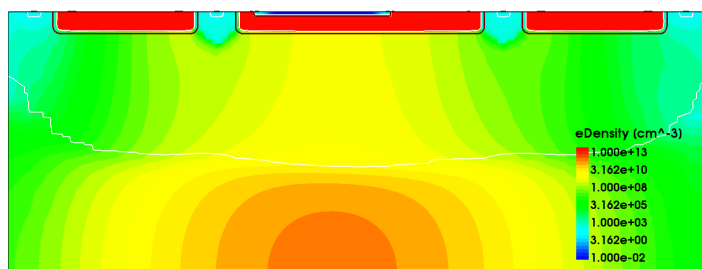
**Figure 5.8** – a) *mip* passing through the center of the pixel for a simulated device with a resistivity of  $\rho = 80 \, \Omega\text{cm}$  biased with  $HV_{bias} = -50 \, \text{V}$  b) Induced current as a function of the time for different resistivities. The bias voltage is  $HV_{bias} = -50 \, \text{V}$  c) collected electrons as a function of the time.



(a)



(b)



(c)

**Figure 5.9** – Electrons distribution at different time intervals for a device with a resistivity of  $\rho = 1000$ ,  $HV_{bias} = -50$  V. a)  $\sim 1$  ns after the interaction. b)  $\sim 5$  ns after the interaction c)  $\sim 30$  ns after the interaction.

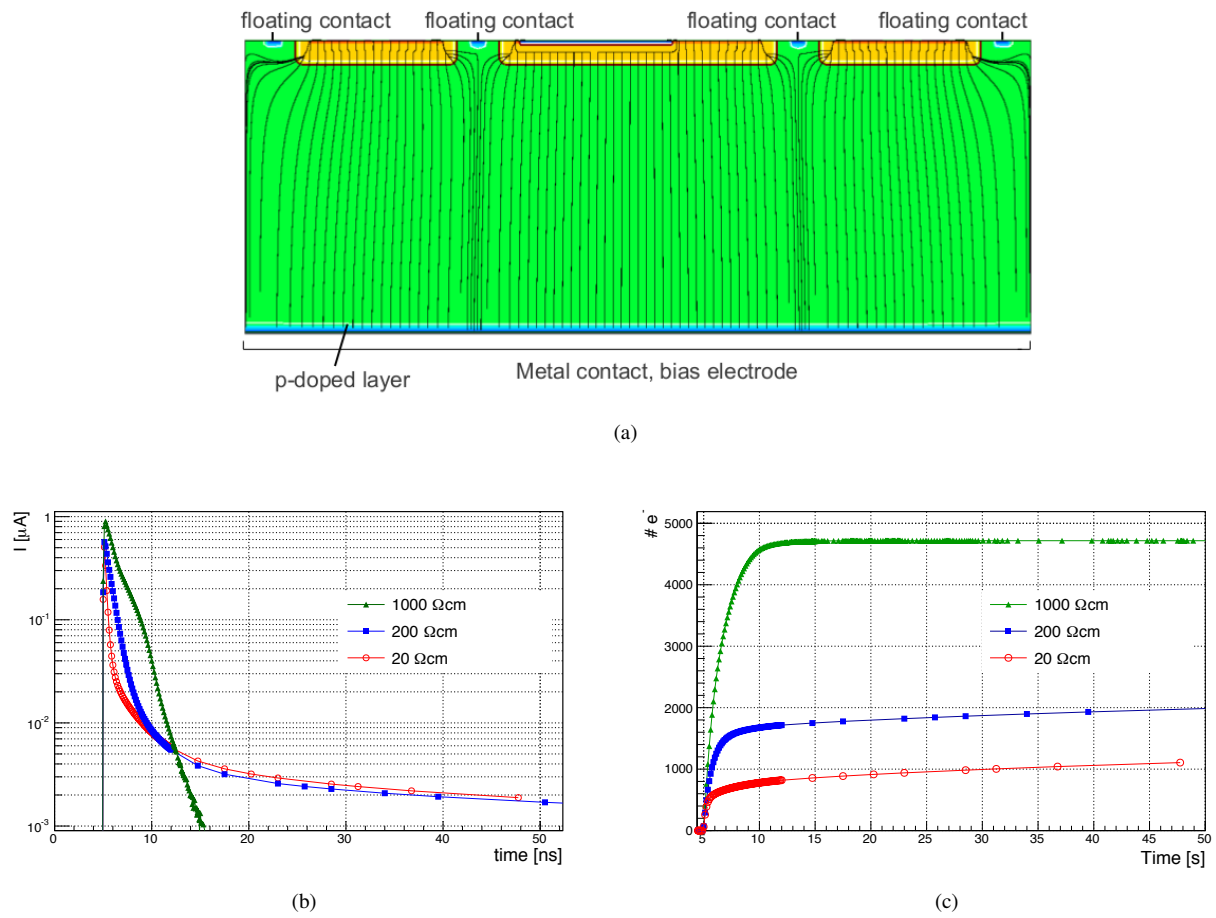


**Figure 5.10** – a) Field lines of a simulated device with a resistivity of  $\rho = 1000 \Omega\text{cm}$  biased from the back. b) Induced current as a function of the time for different resistivities. The bias voltage is  $HV_{bias} = -50 \text{ V}$  b) collected electrons as a function of the time.



---

## Conclusions

---

New radiation hardness particle detectors, based on the High-Voltage CMOS (HV-CMOS) technology have been proposed as a pixel sensor for the new tracker (ITk) of the ATLAS detector at the HL-LHC.

In our study, the well known FE-I4 readout chip is glued onto the HV-CMOS sensor so that the sensor electrodes and the input pads of the readout channels form capacitors. This assembly is called Capacitively Coupled Pixel Detector (CCPD).

During the realization of this thesis, I have contributed to the most recent test-beam measurements of several CCPD prototypes. I have also been involved in TCAD simulations for the optimization of the design of the upcoming CCPD prototype.

Results of the test-beam measurements show an efficiency of 99.5 % for the non-irradiated CCPD and 96.5 % for the sample irradiated at  $10^{15} n_{eq}/cm^2$ . The timing distributions of the analyzed CCPDs show long tails. For the non-irradiated prototypes an efficiency of around 99 % is reached in  $\sim 15$  b.c. For the irradiated samples, instead, the overall efficiency is reached in  $\sim 8$  b.c. As a result of our analysis we have addressed these features to two different effects: a slow diffusion component, which mostly affects the non-irradiated prototypes, and a time-walk effect which originates at the on-chip pre-amplifier. In view of these results a compensated time-walk comparator is foreseen to be adapted to the on-chip electronics of the new prototypes.

TCAD simulations of the upcoming CCPD prototype have been performed for different substrate resistivities: 20  $\Omega\text{cm}$ , 80  $\Omega\text{cm}$ , 200  $\Omega\text{cm}$  and 1000  $\Omega\text{cm}$ . We observed that simulated devices, with resistivities of 200  $\Omega\text{cm}$  and 1000  $\Omega\text{cm}$ , present a low electric field in the deep-bulk region leading to a slower collection time and a lower collected signal compared to the devices with resistivities of 20  $\Omega\text{cm}$  and 80  $\Omega\text{cm}$ .

We have compared these results with those obtained with a back-bias solution. In this case, for higher resistivity values we observed a larger collected signal and, in particular, for a simulated device with a resistivity of 1000  $\Omega\text{cm}$ , biased at 50 V, the charge is fully collected in  $\sim 10$  ns.

A new prototype designed to fulfill the requirements for being considered a valid technology for the ITk (99 % efficiency in the first 2 bunch crossing) is foreseen for September 2015. The properties of the upcoming CCPD prototype will be studied in detail in test-beam, simulations and laboratory. The test-beam analysis and the simulation models developed for this thesis represent a starting point for future, profitable, studies aiming to demonstrate the feasibility of the CCPD as a pixel sensor for the ITk.





In the chapter 4, the peaked structure observed in the residual distributions of the telescope planes, have been successfully reproduced using simulations. In this appendix a preliminary study will be discussed, giving elements about the understanding of the effect of such peaks in the resolution of the telescope. In particular, we aim to understand how sub-pixels region are identified after the reconstruction procedures at the DUT. The simulation model used for this study has been already presented in the chapter 4.

Figure 3.2 shows the in-pixel occupancy of the DUT for real data (the pixel size is  $250 \times 100 \mu m^2$  because of a merging, along the Y axis, of two FE-I4 pixels). The distribution presents five regions separated by  $50 \mu m$  because of the effect previously mentioned. A region of interest within each single pixel has been defined in the DUT at a simulation level, as shown in figure 6.2(a) and 6.3(a). The two regions of interest have been simulated to study separately the two measuring directions (X and Y respectively). These simulated data have been reconstructed as shown in figures 6.2(b) and 6.3(b). We note that the regions at the edges of the simulated sensor are reconstructed in the in-pixel efficiency map. On the other hand, the simulated regions are increasingly less visible after the reconstruction. As discussed in chapter 4, the simulated telescope is perfectly aligned and the beam has been simulated with no angular distribution. Therefore, the fact that some regions are visible after the reconstruction could be explained by multiple scattering effects. A scattered particle can fire different pixels in different planes of the telescope, thus changing the slopes of the reconstructed track. In particular, a particle that passes near the edge of the pixel will be more easily scattered at the adjacent pixel in the following plane compared to another particle that passes near the centre of the pixel. Therefore, in this simple model, the leading quantity in the reconstruction of sub-pixel structure is the distance that the structure has from the centre of the pixel.

We conclude that, thanks to the multiple scattering, it is possible to identify, within the limits discussed above, the sub-pixel structures after the reconstruction.

Even though with a simple configuration (e.g. flat beam-profile, perfectly aligned setup), the simulation studies presented in this appendix have provided a first qualitative description of sub-structure identification. However, in order to get more quantitative results, a more realistic simulation is needed, e.g. by including a realistic beam-profile, a software digitization module (realistic charge sharing effects, affecting cluster-size distribution), and by the implementation of various types of module misalignments (translations and rotations).

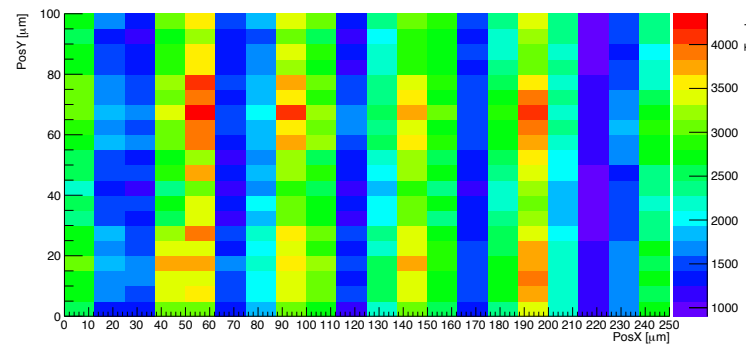
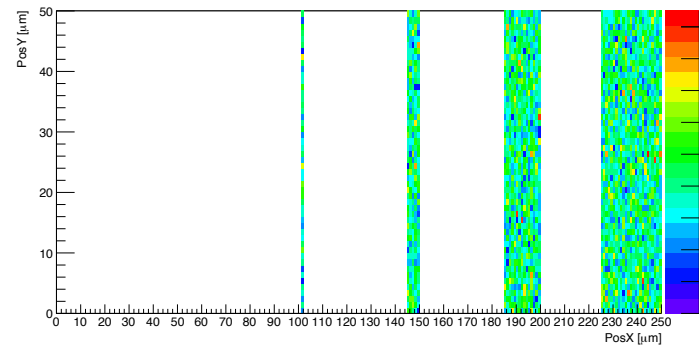
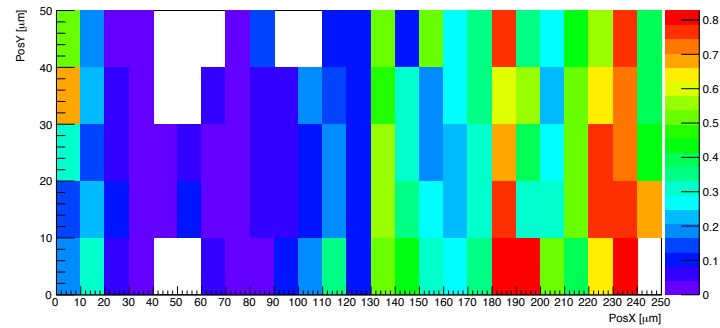


**Figure 6.1** – In-pixel occupancy distribution for real data. Five regions separated by  $50 \mu m$  are present.

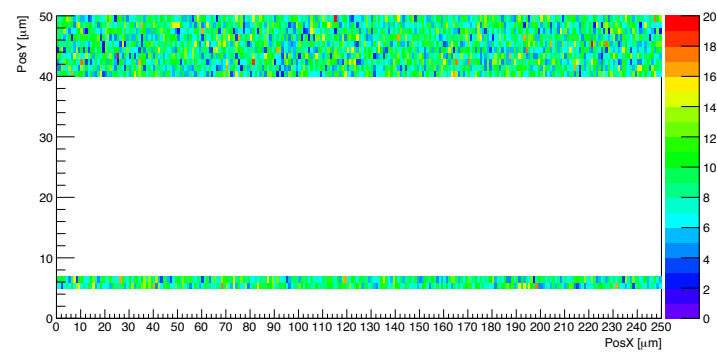


(a)

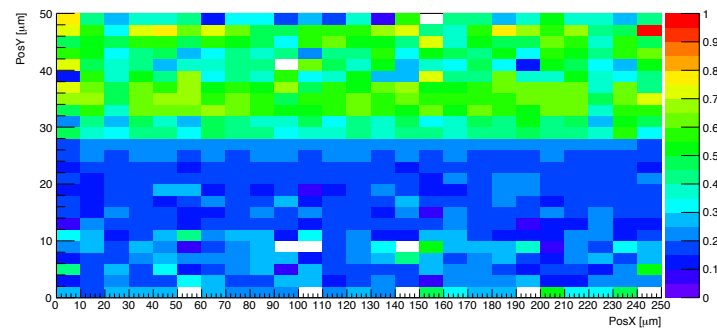


(b)

**Figure 6.2** – a) Simulated in-pixel occupancy distribution. b) Reconstructed in-pixel efficiency map.



(a)



(b)

**Figure 6.3** – a) Simulated in-pixel occupancy distribution. b) Reconstructed in-pixel efficiency map.



---

## Bibliography

---

- [1] ATLAS collaboration. Letter of Intent Phase-II Upgrade. *CERN-2012-022, LHCC-I-023*, 2012.
- [2] ATLAS collaboration. The ATLAS Experiment at the CERN Large Hadron Collider. *JINST 3 S08003*, 3, 2008.
- [3] I. Peric. Active pixel sensors in high-voltage CMOS technologies for ATLAS. *JINST C08002*, 2012.
- [4] V. Rüdiger et al. (CERN). *The CERN Large Hadron Collider : Accelerator and Experiments*. CERN, 2009.
- [5] O. Brüning et al. (CERN). *LHC Design Report 2004*. CERN, 2004.
- [6] The ATLAS collaboration. *ATLAS inner detector : Technical Design Report, 1*. CERN, 1997.
- [7] PPS 3D Collaborations P. Grenier, on behalf of the ATLAS IBL. Silicon sensor technologies for the atlas ibl upgrade. *Physics Procedia*, 37, 2012.
- [8] The ATLAS collaboration. *ATLAS Insertable B-Layer Technical Design Report*. CERN, 2010.
- [9] The ATLAS IBL Collaboration. Prototype ATLAS IBL Modules using the FE-I4A Front-End Readout Chip. *JINST, arXiv:1209.1906*, 37, 2012.
- [10] The ATLAS collaboration. *ATLAS Magnet System Technical Design Report*. CERN, 1997.
- [11] The ATLAS collaboration. *ATLAS tile calorimeter : Technical Design Report*. CERN, 1996.
- [12] The ATLAS collaboration. *ATLAS liquid-argon calorimeter : Technical Design Report*. CERN, 1996.
- [13] The ATLAS collaboration. *ATLAS muon spectrometer : Technical Design Report*. CERN, 1996.
- [14] H. Bethe und J. Ashkin. *Experimental Nuclear Physics*, ed. E. Segré, J. Wiley, New York, 1953, p. 253.
- [15] K.A. Olive et al. (Particle Data Group). *The Review of Particle Physics*, *Chin. Phys. C*, 38, 090001, 2014.
- [16] B. Rossi. High energy particles. *Prentice-Hall, Inc., Englewood Cliffs, NJ*, 1952.
- [17] Landau. L. *J. Exp Phys. (USSR)*, 8, p. 201, 1944.
- [18] Vavilov. P.v. *Sov. Phys. JETP*, 5, 749, 1957.
- [19] Fischer P. Rohe T. Wermes N. Rossi, L. *Pixel Detectors, From Fundamentals to Applications*. Springer, 2006.
- [20] F. Hartmann. *Evolution of silicon sensor technology in particle physics*. Springer, 2009.

- 
- [21] C. Kittel. *Introduction to Solid State Physics, 8th edition, 2004.*
  - [22] W. Shockley. Currents to conductors induced by a moving point charge. *J. of Applied Physics* 9 (10): 635., 1938.
  - [23] Synopsis. *Sentaurus Device User Guide, Version I-2013.12, December 2013.*
  - [24] W. Shockley and W. T. Read. Statistics of the recombinations of holes and electrons. *Phys. Rev.*, 87 , pp. 835–842., 1952.
  - [25] M. Moll. *Radiation Damage in Silicon Particle Detectors, microscopic defects and macroscopic properties. PhD Thesis, 1992.*
  - [26] R. Wunstorf. *Systematische Untersuchungen zur Strahlenresistenz von Silizium-Detektoren für die Verwendung in Hochenergiephysik-Experimenten. PhD Thesis , 1992.*
  - [27] I. Peric, C. Kreidl and P. Fischer. Particle pixel detectors in high-voltage CMOS technology. *Nuclear Instruments and Methods in Physics Research, A* 650 (2011) 158–162, 2010.
  - [28] M. Backhaus. *High bandwidth pixel detector modules for the ATLAS Insertable B-Layer, PhD Thesis, 2014.*
  - [29] S. Feigl On behalf of the HV-CMOS collaboration. Performance of capacitively coupled active pixel sensors in 180 nm HV-CMOS technology after irradiation to HL-LHC fluences. *JINST*, 2013.
  - [30] I. Peric. *Overview of HV/HR-CMOS Pixel Sensors, slides, 2014.*
  - [31] A. F. Zarnecki and P. Niezurawski. *EUDET Telescope Geometry and Resolution Studies, 2011.*
  - [32] R. Bartoldus et al. *High Bandwidth DAQ RD for ATLAS Upgrade, 2011.*
  - [33] L. Carlson. *ATLAS HSIO DEVELOPMENT BOARD TESTING, 2010.*
  - [34] A. Gorisek G. McGoldrick M. Cerv. Synchronized analysis of testbeam data with the judith software. *Nuclear Instruments and Methods in Physics Research, A*, 140-145, 2014.
  - [35] B. Ristic. *The FE-I4 telescope, slides, DESY Hamburg, 2015.*
  - [36] S. Agostinelli et al. Geant4—a simulation toolkit. *Nuclear Instruments and Methods in Physics Research*, 506, 2003.
  - [37] M. Benoit. *Étude des détecteurs planaires pixels durcis aux radiations pour la mise à jour du détecteur de vertex d'ATLAS, PhD Thesis, 2011.*
  - [38] André Fortin. *Les éléments finis : de la théorie à la pratique, 2014.*
  - [39] E. Vilella. *AMS H35 demonstrator design status/plans, internal ATLAS slides, 2015.*
  - [40] S. Agostinelli et al. Modeling of carrier mobility against carrier concentration in arsenic-, phosphorus-, and boron-doped silicon. *Electron Devices, IEEE*, 30, pp. 764 - 769, 1983.
  - [41] C. Canali et al. Electron and hole drift velocity measurements in silicon and their empirical relation to electric field and temperature. *IEEE Transactions on Electron Devices*, vol. ED-22, no. 11, pp. 1045–1047, 1975.
  - [42] N. D. Arora D. J. Roulston and S. G. Chamberlain. Modeling and measurement of minority-carrier lifetime versus doping in diffused layers of n+-p silicon diodes. *IEEE Transactions on Electron Devices*, vol. ED-29, no. 2, pp. 284–291, 1982.
  - [43] J. W. Slotboom. The pn-product in silicon. *IEEE Transactions on Electron Devices, Solid-State Electronics*, vol. 20, no. 4, pp. 279–283, 1977.